Stiffness of granular soils under long-term multiaxial cyclic loading

MANDOLINI A., DIAMBRA A. & IBRAIM E.

Article manuscript submitted to Géotechnique

Re-submitted on: 12th June 2020

Alessandro Mandolini
Geotechnical Engineer
Lloyd's Register
email: alessandro.mandolini@lr.org
Formerly, Department of Civil Engineering, University of Bristol, Bristol, UK

Andrea Diambra [corresponding author]
Senior Lecturer
Department of Civil Engineering, University of Bristol, Bristol, UK
Phone: +44 0 117 331 5600; email: andrea.diambra@bristol.ac.uk
https://orcid.org/0000-0003-4618-8195

Erdin Ibraim
Reader
Department of Civil Engineering, University of Bristol, Bristol, UK
Phone: +44 0 117 331 7534; email: erdin.ibraim@bristol.ac.uk
http://orcid.org/0000-0003-1077-0546

Number of words: approx. 5600 (excluding abstract, references and captions)

Number of figures: 22

Number of tables: 2

Abstract

Geotechnical infrastructures may be subjected over their lifetime to long-term loading cycles of varying amplitude, frequencies and direction as a result of the combination of environmental and operational processes. Soil elements surrounding the foundations of these geotechnical systems are in turn subjected to complex six-dimensional stress paths, invariably involving rotation of principal stress axes. Changes of the soil's mechanical properties can lead to changes of the overall structure dynamics as well as to an accumulation of irreversible deformations. However, the evolution of the soil's response and stiffness under complex long-term cyclic loading scenarios is neither well known nor adequately understood. In contrast to the conditions imposed by standard laboratory tests, this research used a Hollow Cylinder Torsional Apparatus (HCTA) to explore the evolution of the small-strain stiffness of a granular soil under long-term multiaxial drained stress cycles (up to about $6x10^5$). Granular soil samples were subjected to stages of regular low amplitude stress cycles at different anisotropic stress levels interspersed by periodic large amplitude cyclic loops. A high resolution local strain measurement system was employed to determine the vertical Young's modulus and shear modulus, both attained in a HCTA at different stages of the testing. It was found that low amplitude multiaxial stress cycles, involving continuous rotation of principal stress axes, caused a degradation up to about 20% of these elastic soil properties. Within 10^4 to $2x10^4$ cycles, the degraded stiffnesses reached a stable value which was maintained up to at least $8x10^4$ cycles. The stiffness degradation was more pronounced for the shear modulus rather than the vertical Young's modulus of the soil.

1 Introduction

Environmental (e.g. wave or wind), traffic and operational (e.g. mechanical movement or vibration) live actions on geotechnical structures may result in a very large number of small or high amplitude loading cycles transmitted to the foundation and the surrounding soil. For example, during the 20-25 years design life, the soil around the foundation of offshore renewable energy structures, such as wind turbines, is subjected to about 10 to 100 million cycles of varying amplitudes, directions and frequencies. Similar long-term cyclic loading is also typical of offshore oil and gas platforms, railway and highway structures such as embankments and bridges, and foundations for vibratory machines, among others (Andersen 2009; Corti et al. 2017; Liu et al. 2018). The geotechnical design of these structures is generally governed by ultimate, serviceability and fatigue limit states, for which the cyclic accumulation of soil deformation and the evolution of the soil stiffness are primary governing factors. The elastic soil characteristics may be particularly important for dynamically sensitive structures, such as wind turbines and vibratory machines, which need to be designed within narrow natural frequency ranges and against strict fatigue criteria (Randolph and Gourvenec, 2010).

Many studies have considered the cyclic response of soils through standard axisymmetric (triaxial) or simple shear loading conditions investigating the influence of many variables such as soil type and density, average stress level, cyclic mode (one or two way), cyclic amplitude and drainage conditions (e.g. Wichtmann et al. 2004a, 2005, 2007a; Escribano et al., 2018). Wichtmann et al. (2004b) found that application of up to 10^6 cycles in a conventional triaxial tests has not a significant impact on the vertical Young's modulus of a granular soil (measured through bender elements), irrespective of the average stress level, cyclic stress amplitude and relative soil density. However, in real situations the stress paths are more complex and re-orientation of principal stress and strain axes are also expected to occur for a wide range of geotechnical structures, including embankments, piles and shallow foundations (Arthur et al. 1980) under most types of loading. Sustained multi-directional cyclic loading (such as that induced by environmental, traffic and operational processes) can cause continuous, long-term soil cyclic re-orientation of principal stress and strain axes. Wichtmann et al. (2007b) found that the direction of multi-directional simple shear does not considerably affect the strain accumulation rate, but sudden changes of the loading direction can temporarily increase the strain accumulation rate. Tong et al. (2010) demonstrated that accumulation of plastic deformations can be solely triggered by continuous rotation of principal stress axes without changes of magnitude of the principal stresses (application of circular stress paths in a hollow cylinder torsional apparatus). Despite this evidence, experimental studies on soil response under long-term multiaxial cyclic loading are still rather limited and often based on the employment of 'external' strain measurement systems ('external' as opposed to 'local' measurements made on soil samples, Jardine et al. (1984), Baldi et al. (1988), Shibuya et al. (1992), Tatsuoka et al. (1994)).

This paper aims to expand the current state of knowledge of cyclic soil behaviour by investigating how small-strain stiffness properties of granular soils are affected by the application of a large number of low-amplitude multiaxial loading cycles, which trigger cyclic re-orientation of principal stress axes. The study is carried out using the Hollow Cylinder Torsional Apparatus (HCTA) equipped with a high-resolution local strain measurement system and the focus is on the assessment of the vertical Young's modulus, E_z, and shear modulus, $G_{\theta z}$, tracking their evolution with long-term cyclic loading. In the HCTA, cyclic loading is applied through variation of the axial effective stress $\Delta\sigma'_z$ and/or torsional stress $\Delta\tau_{\theta z}$. Low-amplitude cycles defined as cycles having a normalised stress amplitude, $\Delta\sigma'_z/p'$ and/or $\Delta\tau_{\theta z}/p'$, less than about 10%, where p' is the pre-cyclic mean effective isotropic stress. Representation of stresses in a (z, r, θ) cylindrical coordinate system for a hollow cylinder sample is given in Figure 1.

While the stress state around geotechnical structures is complex, this studyhas considered two distinct drained monotonic stress paths: one purely axial and the other one purely torsional, upon which, at various stress and strain states, long-term low-amplitude drained cyclic loading is applied. These pre-

cyclic stress conditions are schematically shown by the point "A" for the pure axial stress path and point "T" for the pure torsional stress path in Figure 2, which uses the conventional $\tau_{\theta z}$ vs. $(\sigma'_z-\sigma'_\theta)/2$ stress plane for HCTA plots. σ_z, σ_θ and $\tau_{\theta z}$ are the axial, circumferential and shear stresses respectively as defined for a hollow cylinder specimen (Figure 1). The angle β in Figure 2 defines the relative orientation between the cyclic loading path and the pre-cyclic monotonic loading path in the $\tau_{\theta z}$ vs. $(\sigma'_z-\sigma'_\theta)/2$ stress plane. During the axial and pure torsional testing, the long-term low-amplitude stress cycles were also periodically interspersed with large axial and pure torsional unload-reload cycles, respectively. The effect of the application of the long-term cycles on the small strain stiffness properties (vertical Young's and shear moduli) of the sand at the pre-cycling A and T stress conditions was monitored at regular intervals. Long-term cyclic stress conditions up to about $6{\cdot}10^5$ cycles have been simulated within a single test.

2 HCTA, material, sample preparation and small strain measurement system

2.1 HCTA

The HCTA at Bristol University allows the testing of hollow cylinder-shaped samples with an outside diameter of 100mm, an inner diameter of 60mm and height of 200mm. The apparatus permits independent control of four load components: axial load (W), axial torque (T) applied through the rigid end platens and two confining pressures on the specimen inner and outer flexible lateral surfaces, p_i and p_o, respectively (Figure 1a). The relationships for the calculation of the average stresses (axial σ_z, radial σ_r, circumferential σ_θ and shear $\tau_{\theta z}$ as shown in Figure 1b) and strains (axial, ε_z, radial, ε_r, circumferential, ε_θ and shear, $\gamma_{\theta z}$) follow Hight et al. (1983), Miura et al. (1986) and Vaid et al. (1990). Mandolini et al. (2019) provide a full account of these relationships together with details of the measurement systems employed for their reduction. Corrections due to the membrane's resistance to the applied axial, radial and shear stress have been accounted for using the method suggested by Tatsuoka et al. (1986). The volume changes due to membrane penetration were found to be negligible and no correction was applied.

The stress state of a representative soil element can be represented by the mean effective stress, p', the generalised deviatoric component of stress, q, and the angle between the major principal stress direction and vertical, z-axis, α_σ:

$$p' = \frac{\sigma'_z+\sigma'_\theta+\sigma'_r}{3} = \frac{\sigma'_1+\sigma'_2+\sigma'_3}{3} \quad (1)$$

$$q = \sqrt{\frac{(\sigma'_z-\sigma'_r)^2+(\sigma'_r-\sigma'_\theta)^2+(\sigma'_\theta-\sigma'_z)^2}{2} + 3{\tau_{\theta z}}^2} \quad (2)$$

$$\alpha_\sigma = \frac{1}{2}\, tan^{-1}\left(\frac{2\tau_{\theta z}}{\sigma'_z - \sigma'_\theta}\right) \quad (3)$$

where σ'_1, σ'_2, and σ'_3 are the major, intermediate and minor principal effective stresses, respectively (Figure 1c).

2.2 Material and sample preparation

The experimental testing has been conducted on Hostun RF (S28) sand. This sand is a standard European material for laboratory testing with a high siliceous content (SiO_2) of 98%, angular to sub-angular grains (Ibraim et al., 2012), mean grain size, D_{50}=0.38 mm, coefficient of uniformity, $C_u=D_{60}/D_{10}$=1.9 and coefficient of gradation $C_g=(D_{30})^2/(D_{10}D_{60})$=0.97. The maximum and minimum void ratios determined according to the British standards (BS EN ISO 17892-2:2014) are e_{max}=1.00 and e_{min}=0.62, respectively. The specific gravity is G_s=2.65.

The HCTA samples were prepared by dry deposition through a funnel ensuring zero height fall. Following the sand deposition, the sample mould was subjected to a vertically dominated vibration imposed by a shaker under a frequency of about 50 Hz and acceleration of 2g, under a constant light soil surcharge of 28 kPa provided by a vertically guided hollow circular top cap.Once the target density was achieved, the sample was sealed and subjected to a 20 kPa vacuum pressure prior to the removal of the mould. The sample was then transferred inside the HCTA and saturated using CO_2 together with de-aired water and back pressure up to 300 kPa. Values of Skempton's coefficient of at least 0.97 were systematically measured. Further details of the sample preparation procedure employed can be found in Mandolini (2018).

2.3 Small strain: measurement system and procedures

The evaluation of the small strain stiffness in the HCTA was provided by a local measurement system consisting of six high-resolution non-contact displacement transducers (based on Eddy current effect) each with a measurement range of 2mm and resolution better than 0.1 µm (Ibraim et al. 2012). A schematic representation of the arrangement of the non-contact transducers around the sample including the targets is provided in Figure 3. Aluminium plates are attached to circular rings attached in turn to the sample measurement points, based on solutions proposed and tested by Duttine et al. (2007) and Ezaoui and Di Benedetto, (2009)., The sensors S1 and S2 monitored the vertical movements of the local measurement points to measure the vertical strains (ε_z) over the middle third of the sample. The sensors S3 and S4 monitored the circumferential movements of the targets to deduce the shear strains ($\gamma_{\theta z}$). The sensors S5 and S6 provided the outer radial sample variations. The latter sensors pointed towards aluminium foil targets placed on the sample's side of the outer membrane - in direct

contact with the sand. The variation of the outer radius was an average of these two measurements. The small strain variations of the sample inner radius were calculated from the volume changes of the inner cell combined with the vertical small strain variations.

The soil elastic vertical Young's, E_z, and shear, $G_{\theta z}$, moduli properties were determined using the conventional procedure of applying successive quasi-static unload-reload cycles, $\Delta\sigma'_z$ and $\Delta\tau_{\theta z}$ respectively, of small amplitude at different stress levels (called investigation points, A and T in Figure 2 for this study). Owing to the low measurement range of the non-contact sensors, complex technical solutions, detailed in Ibraim et al. (2012), were developed to allow, if necessary, the re-positioning of each transducer from outside the confining cell. The relocation of the sensors permitted the use of the local system at any investigation point along any stress path taking advantage of their high resolution.

Examples of time-histories of typical small strain cyclic loading $\Delta\sigma'_z$ =±5 kPa and $\Delta\tau_{\theta z}$ =±3.1 kPa (stress perturbations are defined from peak to trough points throughout the paper) applied at the investigation points for soil stiffness evaluation and the corresponding measured strains $\Delta\varepsilon_z$ and $\Delta\gamma_{\theta z}$ given by the local measurement system, are shown in Figures 4a and 4d, and Figures 4b and 4e, respectively. At least 10 stress-controlled cycles at a frequency of 0.005Hz were applied and data recorded at a sampling rate of 20 measurement points/second. The quality of the stress control and the high accuracy of the measurement system, able to resolve strain levels lower than 10^{-5} m/m, are also highlighted in the Figures 4c and 4f. No signs of creep deformation effects were also observed since systematic creep test stages were conducted prior to small-strain investigation. The axial and shear strains showed an excellent repeatability of the responses for the successive cycles and the superposition of the stress-strain relationships was identical and linear with no hysteresis or energy dissipation, suggesting that these strain levels were below the elastic limits for this material. No systematic attempt to determine the elastic strain limits of this sand by the application of small-strain cycles of various amplitudes was done. However, the elastic limit was assessed based on the monotonic loadings as will be shown on the following section. The quasi-elastic Young's, E_z, and shear, $G_{\theta z}$, moduli were calculated from the slopes of the stress-strain cycle responses, as shown in the Figures 4c and f.

3 Testing programme

The experimental programme aimed to investigate the effect of applying long-term low-amplitude stress cycles on the elastic properties (Young's and shear moduli) of a granular material. As discussed above, the study considered two distinct stress paths: pure axial and pure torsional, as shown in Figure

2, along which, at different stress levels, low amplitude long-term stress cycles were applied. The experimental programme included eight tests, divided in two categories:

- The first four tests (type I) followed the stress history schematically represented in Figure 5a and the applied test conditions for these four tests are given in Table 1. The stress paths in the $\tau_{\theta z}$ versus $(\sigma'_z - \sigma'_\theta)/2$ plane are shown in Figure 5b. All four HCTA samples were firstly isotropically consolidated to an effective stress of 100 kPa. Then the samples were brought monotonically to different axial (A-β0 and A-β90 tests) or pure torsional (T-β0 and T-β90 tests) stress levels while the inner and outer cell pressures were kept constant, Figure 5b. At each stress level, after creep deformations allowed for several hours were negligible, the samples were then subjected to stages of about or in excess of 3000 axial ($\Delta\sigma'_z$=±5 kPa, tests A-β0 and T-β90) or torsional ($\Delta\tau_{\theta z}$=±5 kPa, tests A-β90 and T-β0) stress cycles (c1 to c6 in Figure 5a), whilst still keeping the inner and outer cell pressures constant. These corresponded to normalised cyclic stress amplitudes $\Delta\sigma'_z/p'$ and $\Delta\tau_{\theta z}/p'$ varying between *0.038* and *0.055.* In the name of the tests, "0" or "90" indicate the value of the angle β of the relative orientation of the cyclic loading with respect to the pre-cyclic monotonic stress path (Figure 2). $\Delta\alpha_{cyc}$ in Table 2 represents the induced cyclic re-orientation of principal stress axis for each cyclic stage. Figure 5b provides the values of the mobilised friction angles, ϕ'_m, determined using a Matsuoka-Nakai multiaxial failure criterion (Matsuoka and Nakai, 1974), corresponding to each pre-cyclic axial or torsional stress level. Applicability of the Matsuoka-Nakai failure criterion for Hostun sand under probing stress paths in the HCTA was demonstrated by Mandolini et al. (2019). The elastic Young's, E_z, and shear, $G_{\theta z}$, moduli were systematically measured before the start ($E_{z(i)}$ and $G_{\theta z(i)}$) and at the end ($E_{z(f)}$ and $G_{\theta z(f)}$) of each cyclic stage following the procedure detailed in section 3.3.

- The remaining four tests (type II) focussed on the investigation of the evolution of small strain stiffness under a much higher number of stress cycles, as well as different cyclic stress amplitudes and directions (Figure 6). These tests considered also pure axial (tests A-β90 (L1), A-β90 (L2) and A-β90β0) or pure torsional (test T-β*) stress paths. For the latter test, values of the angle β different from 0° and 90° were applied. The stress paths and cyclic stress sequence applied are also schematically represented in Figure 6. Isotropic consolidated HCTA samples to an effective stress of 100 kPa were loaded to an axial or a pure torsional stress levels, maintaining the inner and outer cell pressures constant. At these stress levels, after creep was allowed for several hours until creep strain was considered negligible , the samples were subjected to several long-term axial and/or torsional cyclic loading stages (of amplitudes

$\Delta\sigma'_z$ and/or $\Delta\tau_{\theta z}$ between ±3 kPa and ±12 kPa, corresponding to normalised cyclic stress amplitudes $\Delta\sigma'_z/p'$ and $\Delta\tau_{\theta z}/p'$ between 0.02 and 0.10) of up to $8x10^4$ cycles, whilst still keeping the inner and outer cell pressures constant. Between consecutive low amplitude cyclic stages, the specimens were subjected to some large unload-reload cyclic loops. Overall, a total number of low amplitude cycles between $1.3x10^5$ and $6.5x10^5$ were applied over a duration of about six months for the longest test, test A-β90β0. Details of these four tests are given in Table 2, while Figure 6b shows their $\tau_{\theta z}$ versus $(\sigma'_z - \sigma'_\theta)/2$ stress paths. Exploration of the small strain stiffness were systematically carried out at regular intervals within each cyclic stage, however, only the values of the elastic Young's and shear moduli measured before the start ($E_{z(i)}$ and $G_{\theta z(i)}$) and at the end ($E_{z(f)}$ and $G_{\theta z(f)}$) of each cyclic stage are reported in Table 2.

All the low-amplitude cyclic loading in all these tests were conducted at a frequency of 0.05 Hz. Previous research showed that loading frequencies of this magnitude do not affect the magnitude of elastic stiffness moduli in granular soils (Tatsuoka et al., 1986; Wichtmann et al., 2005). While all the tests were supposed to be carried out on specimens at a nominal void ratio of 0.82 (corresponding to a relative density of about 52%), values of the void ratios between 0.814 and 0.833 (corresponding to relative densities between 51% and 56%) were achieved at the end of the first isotropic consolidation stage for each test. The evolution of the void ratios, based on the global volume measurement system, is provided in Tables 1 and 2 for the consecutive cyclic stages of each test. Further information on the general monotonic behaviour, small strain stiffness and large amplitude cyclic response of the Hostun sand, including critical state parameters, can be found in Doanh et al. (1997), Doanh and Ibraim (2000), Duttine et al. (2007), Ezaoui and Di Benedetto (2009), Ibraim et al. (2011), Corti et al. (2016) and Escribano et al. (2018), among others.

4 Experimental results

4.1 Test type I

The stress-strain responses for all the type I tests are presented in Figure 7. Along each stress path of the tests, six cyclic stages c1-c6 were applied at different stress and strain conditions. The amplitudes of the applied stress cycles were $\underline{\Delta\sigma'_z}$=±5 kPa or $\Delta\tau_{\theta z}$=±5 kPa. The maximum mobilised angles of friction for the tests did not exceed 29° based on Matsuoka and Nakai (1974). The strains reported in Figure 7 were determined from the global external displacement and rotational transducers and remained relatively small under 0.7% for axial strain and 1.5% for shear strain. Figure 8 shows the evolution of the secant Young's and shear moduli normalised respectively with the maximum E_{z0} and $G_{\theta z0}$ moduli with the strain levels for the initial loading parts of all type I tests for which the local strain measurement system was operational. The axial and shear stiffnesses exhibited a plateau and its limit

allowed the definition of an elastic strain limit somewhere between 2 and 4x10^{-5} (m/m). Although the cyclic stress level applied at different investigation points was relatively small, some limited accumulation of axial and torsional strains during each cyclic stage could be observed as a result of possible compliance errors in the system or due to sample end effects. However, when the measurements were recorded by the local strain measurement system, a much lower strain accumulation was detected. For example, Figure 9 shows all the components of the accumulated strains for each single stage from c1 to c6 of the test T-β90 showing that all strain levels remained below about 0.02% for the maximum number of 3780 cycles applied within each cyclic stage.

The small-strain Young's and shear stiffness measurements conducted at the beginning and at the end of each cyclic stage (c1-c6) for all the tests are reported in the 10 and 11, respectively. The effect of the void ratio variation was removed by correcting the stiffness values by the void ratio function *f(e)*, already used by Ibraim et al. (2011) for the same sand:

$$f(e) = \frac{(3{,}01-e)^2}{1+e} \quad (4)$$

Within a cyclic stage involving typically a number of 3000 axial or torsional cycles, the corrected stiffness data showed similar initial and final values with ±5% variation in all the tests, with or without cyclic rotation of principal stress axes. The same observation applies for the longer cyclic stages conducted up to about 12000 cycles (stage c5 of A-β0 test and stage c6 of A-β90 test). For the cyclic stages conducted at the same stress conditions within the same test, no differences between stiffness values were observed neither for the corrected Young's modulus nor shear modulus. However, the effect of the effective normal stress in the direction of loading (σ'_z) at which the Young's modulus (E_z) and shear modulus ($G_{\theta z}$) were determined for the A-β0 and A-β90 tests appears clearly as shown in 10a and b and 11a and b, respectively. The data presented in 12a confirmed the power law dependency of the Young's modulus (E_z) on the effective normal stress in the direction of loading (σ'_z), Hardin and Blandford (1989), Hoque and Tatsuoka (1998):

$$E_z = C\, f(e) \left(\frac{\sigma'_z}{\sigma_{ref}}\right)^m \quad (5)$$

where, σ_{ref} is a reference pressure of 1 kPa, the value *C* was found equal to 5.6 for E_z expressed in MPa and the exponent *m* takes a value of 0.52 corroborating previous results on Hostun sand (e.g. Di Benedetto et al. 1999, Ibraim et al. 2011). Conversely, the shear modulus was dependent on the two normal stresses acting on the plane of shearing according to Roesler (1979), Di Benedetto et al. (1999), among others, through a relation of the following type:

$$G_{\theta z} = D\, f(e) \left(\frac{\sigma'_z}{\sigma_{ref}}\right)^{n1} \left(\frac{\sigma'_\theta}{\sigma_{ref}}\right)^{n2} \quad (6)$$

The experimental data fit (Eq. 6) as shown in 12b is obtained by imposing a value of D equal to 2.3 and the equal power coefficients $n1$ = n2 = 0.26 in both stress dependent terms. The void ratio function (Eq. 4) was employed in both relationships (5) and (6).

Although no σ'_z or σ'_θ stress changes occurred at the investigation points for the tests involving pure torsional loading, T-β0 and T-β90, from one cycle stage to another, some changes of the Young's modulus (E_z) and shear modulus ($G_{\theta z}$) values were recorded as shown in Figure 10c and d and Figure 11c and d, respectively. Degradation of $E_z/f(e)$ and $G_{\theta z}/(f(e)$ with the application of the shear stress, $\tau_{\theta z}$, could be also observed for both tests in Figure 12c and 12d, respectively, in line with other results reported in the literature (HongNam and Koseki, 2005).

4.2 Test type II

Overall stress-strain response

The experimental type II tests involved the application of a much larger number of cycles as well as wider cyclic amplitude ranges compared with the previous type I tests. The overall stress-strain responses for all type II tests are presented in Figure 13. For some technical reasons, some of the unloading parts of the interspersed unload-reload loops were not recorded and Figure 13 shows only the reloading parts of these large cycles. The three type "A" tests are presented in terms of effective vertical stress (σ'_z) versus the conjugate strain (ε_z), while the type "T" test is presented in terms of torsional stress ($\tau_{\theta z}$) versus torsional strains ($\gamma_{\theta z}$). The tests A-β90(L1) and A-β90(L2) followed similar stress paths but the long-term torsional cyclic stages were conducted at different stress levels (Figure 13a and b). Torsional cyclic amplitudes, $\Delta\tau_{\theta z}$, around ±3 kPa were applied in both tests, while for A-β90(L2) test cyclic loading stages with ±5 kPa amplitudes were additionally considered. The sample of the test T-β* experienced long-term combined axial and torsional stress cycle loading of amplitudes $\Delta\sigma'_z$=±5 kPa and $\Delta\tau_{\theta z}$=±5 kPa (Figure 13d). The test A-β90β0 investigated the distinct effect of alternate axial and shear cyclic loading for a range of cyclic amplitudes, as given in Table 2. Figure 14 shows, as an example, a sample of stress-strain shear cycles with stress amplitudes ranging from ±2 kPa to ±12 kPa selected from the beginning of the cyclic stages marked in the figure. While for all these examples the shear strain was based on the local measurement system, the second cycle in the Figure 14 is representative of the small-strain cycles used for the calculation of the shear stiffness. It is noted the appearance of a hysteresis loop for the torsional cycle loading at $\Delta\tau_{\theta z}$ = ±12 kPa indicating potential occurrence of plastic straining and strain accumulation for the stages c1 to c7. Typical accumulations of strains during the application of long-term cyclic stages for the largest torsional cyclic amplitude of ±12 kPa are shown in Figure 15 (test A-β90β0). The rate of accumulated shear strain seemed to be higher for the initial cyclic stages but further cycling showed strain accumulation stabilisation around

a value of 0.08%. However, with the torsional cycling, the axial strain gently continued to accumulate, while the radial and circumferential strains remained, with one exception, unchanged and relatively close to zero.

Small-strain stiffness evolution

The evolution of both E_z and $G_{\theta z}$ moduli during the application of long-term torsional and/or axial cyclic loading (interspersed with large unload-reload loops, of which occurrences are indicated by a vertical dashed line) for all the type II tests is represented in Figure 16. The stiffness evaluation was conducted at different investigation points along the cyclic stages as shown by the markers in the figure. The solid black-filled markers in Figure 16 designate the investigation points just after the creep stages and before the beginning of the cyclic stage, while the white-filled markers indicate all the consecutive small strain investigation points along a cyclic stage. In order to remove the effect of the void ratio and the stress levels between different cyclic stages, the evolution of the small strain Young's and shear moduli (E_z and $G_{\theta z}$) was analysed in terms of corrected terms based on the relationships (5) and (6), as also reported in Figure 16. Decreasing trends of corrected moduli within a cyclic stage was systematically observed for all four tests. Within a single cyclic stage, the evolution of the small strain stiffness showed a drop towards a steady value which was maintained until a very large number of cycles (for example up to about $8x10^4$ cycles in stage c2 of the test A-β90β0 in Figure 16c). The magnitude of the stiffness drop during the cyclic loading stage was affected by both the type and the amplitude of the cyclic loading history (which are reported in the labels above the double-arrows which bound the cyclic stage). However, the application of large unload-reload loops seemed to restore the initial stiffness values with stiffness moduli (solid black-filled markers in Figure 16) higher than the soil moduli recorded at the end of the previous long-term cyclic stage.

The evolutions of the corrected Young's and shear moduli for cycling stages with identical cyclic stress amplitudes at the same deviatoric stress level are compared in Figure 17. Figure 17a shows all the cyclic stages from c1 to c7 for test A-β90β0, under $\Delta\tau_{\theta z}$=±12 kPa cyclic amplitude. Figure 17b presents data for c1 to c5 successive cyclic stages (combined $\Delta\tau_{\theta z} = \Delta\sigma'_z$ = ±5 kPa cyclic amplitudes) for the test T-β*. The evolution of the corrected moduli is given as function of the specific number of cycles applied during each cyclic stage. The decrease of both corrected stiffness moduli towards their respective steady values took place within the first $2x10^4$ applied cycles. The final steady corrected stiffness values was maintained constant at least until the application of $8x10^4$ and did not change with the large load-unload loop consecutive cyclic stages. Overall, throughout the cyclic stages, the data for the corrected shear modulus showed a lower scatter compared with the corrected Young's modulus.

Influence of cyclic loading characteristics: amplitude and direction

The Figures 18-20 show the evolution of the stiffness moduli $E_{z(i)}$ and $G_{\theta z(i)}$, normalised by the initial value before the application of each cyclic stage, versus the number of cycles applied within each cyclic loading stage. Figure 18 reports the stiffness evolution for samples subjected to the same axial pre-cycling stress state but to cyclic stages characterised by different amplitudes and directions, collecting data from the tests A-β90(L1) and A-β90β0. The largest degradation of both moduli was observed following the application of the largest torsional amplitude $\Delta\tau_{\theta z}$=±12 kPa and was more pronounced for the shear modulus than for the Young's modulus, reaching a steady value at about 80-85% of the initial value (Figure 18b). For this torsional cyclic amplitude, the Young's modulus stabilised around 90-95% of its initial value (Figure 18a). Such levels of stiffness degradation can be related to the generated plastic straining associated to this cyclic amplitude. However, the stiffness degradation may also be related to the cyclic rotation of principal stresses induced by the application of torsional cyclic loading. In fact, torsional cycles of $\Delta\tau_{\theta z}$=±2 kPa, ±3.3 kPa, ±5 kPa and ±12 kPa correspond to a continuous cyclic re-orientations of the principal stress axes of $\Delta\alpha_{cyc}$=±1.3°, ±2°, ±3.2° and ±7.5°, respectively, and a clear trend of stiffness degradation can be detected in Figure 18. The stiffness degradation recorded following the application of axial cyclic loading $\Delta\sigma'_z$=±5 kPa (cyclic re-orientations of principal stress axes, $\Delta\alpha_{cyc}$=0°) showed comparable degradation stiffness moduli levels with that observed for $\Delta\tau_{\theta z}$=±2 kPa (cyclic re-orientations $\Delta\alpha_{cyc}$=±1.3°) corroborating the observed trends. Furthermore, lower stiffness degradation could be observed for the test A-β90(L2) than the test A -β90(L1) also due to a lower cyclic re-orientation of the principal stress axes, $\Delta\alpha_{cyc}$=±1.5° against $\Delta\alpha_{cyc}$=±3.2°, respectively (Figure 19). For the torsional stress path of the test T-β*, the application of combined axial and torsional cycles, inducing continuous re-orientation of principal stress axes around α_σ = 45° of the order of ±2°, seemed to be as damaging as for test type "A" when the rotation of principal stress axes reaches higher values, ±7.5° (Figure 20). For this test type "T", it was also observed a larger degradation of the shear modulus than the Young's modulus under the same cyclic loading conditions. Overall, it could be inferred that the imposed cyclic re-orientation of the principal stress axes may have induced a soil fabric characterised by lower small strain stiffness properties. However, as observed and discussed earlier (see for example results of Figure 16), the application of large monotonic unload-reload loops seemed to restore the previous small strain stiffness properties.

The results of the cyclic stages for all the type II tests are combined in Figure 21 where the values of the stiffness degradation (D_E and D_G for Young's and shear moduli, respectively) are plotted versus the induced cyclic re-orientation of principal stress axes ($\Delta\alpha_{cyc}$) for the corresponding cyclic stage. The stiffness degradations, D_E or D_G, are defined as the difference between the stiffness value before and at the end of the cyclic stage, normalised by the stiffness value before the application of cyclic loading:

$$D_E = \frac{E_{z(i)} - E_{z(f)}}{E_{z(i)}} \; ; \; D_G = \frac{G_{\theta z(i)} - G_{\theta z(f)}}{G_{\theta z(i)}} \quad (7)$$

For both Young's and shear moduli, the data in Figure 21 present a clear increasing trend of stiffness degradation with cyclic re-orientation, more pronounced for the shear modulus (Figure 21b) than the Young's modulus (Figure 21a). Also, as discussed above, a unique trend for both axial and torsional stress paths could not be defined: for torsional stress paths (test type "T"), application of lower $\Delta\alpha_{cyc}$ values induced larger degradation for both moduli than for axial stress paths (test type "A").

Effect of large unload-reload cyclic loop history

Figure 22 presents the evolution of the stiffness moduli ($E_{z(i)}$ and $G_{\theta z(i)}$), before the application of cyclic stage and after the application of the monotonic large unload-reload loops, corrected by the void ratio and the corresponding stress level as per relationships (5) and (6). The x-axis reports the number of applied cyclic stages. Figure 22 combines the information already presented in Figure 16 for the A-type tests. Both plots in Figure 22 clearly show a steady increase of these moduli, although the variation of the moduli is contained within a limited margin of 5-7% of the first measured stiffness after the first monotonic load. This trend, as already discussed above, is opposite to the stiffness degradation induced by the long-term stress cyclic stages which eventually imply the effect of the re-reorientation of principal stress axes and possibly some plastic straining (see for example Figure 18). Considering the case of geotechnical systems subjected to long-term low-amplitude cyclic loading, these results may suggest that the small-strain stiffness of the soil around the foundation may degrade due to the application of long-term cyclic stages, however the soil stiffness may then regain or even increase if large variations of the baseline stress conditions occur.

5 Conclusions

This paper has presented the results of an experimental soil element testing programme, using the Hollow Cylinder Torsional Apparatus, aiming to investigate the variation of soil stiffness (vertical Young's modulus, E_z, and shear stiffness, $G_{\theta z}$) induced by the application of a very large number of low-amplitude multiaxial stress cycles. The experimental programme considered two idealised stress paths - one purely axial and one purely torsional - along which, at different stress levels, low amplitude long-term stress cycles were applied. Some of these long-term cyclic stages also induced the cyclic re-orientation of principal stress axes. The analysis of the experimental results led to the following conclusions:

- For both axial and torsional stress paths, no significant stiffness changes have been observed at a given pre-cyclic stress level when the cyclic loading was limited to about 3000 cycles and the axial and torsional cyclic stress amplitudes were between ±5 kPa.
- Application of longer-term cyclic stages up to $8x10^4$ cycles showed a systematic degradation of the stiffness moduli (either vertical Young's modulus or shear modulus) proportional to cyclic amplitude (especially for larger cyclic amplitudes which may induce plastic straining) and to the related level of re-orientation of the principal stress axes induced by the cyclic loading. However, most of the stiffness degradation took place over the first $1x10^4$ to $2x10^4$ cycles and stabilised thereafter.
- For the same low-amplitude cyclic loading conditions involving cyclic re-orientation of the principal stress axes, larger degradations were systematically observed for the shear modulus rather than the vertical Young's modulus. Under the imposed stress conditions, the shear modulus was found to degrade up to 80%-85% of its initial value, while the Young's modulus values reduced to about 90%-95%.
- For similar levels of cyclic re-orientation of principal stress axes, larger stiffness moduli degradation was observed for the torsional stress path than for the axial stress path tests.
- The application of large unload-reload loops led to a recovery (or even an increase) of the soil stiffness recorded before the application of the long-term cyclic stages for both axial and torsional stress path tests.

Overall, these experimental results provide a benchmark dataset on small strain stiffness evolution, under conditions which differ from standard laboratory tests, supporting the formulation and validation of advanced soil models. Further work aims to consider more complex loading scenarios closer to those experienced by soil elements around the foundations of typical geotechnical structures.

6 References

Andersen, K. H. (2009). Bearing capacity under cyclic loading—offshore, along the coast, and on land. The 21st Bjerrum Lecture presented in Oslo, 23 November 2007. Canadian Geotechnical Journal, 46(5): 513-535.

Arthur, J. R. F., Chua, K. S., Dunstan, T. & Rodriguez, C. J. I. (1980). Principal stress rotation: a missing parameter. Journal of the Geotechnical Engineering Division, ASCE 106 (4): 419–433.

Baldi, G., Hight, D. W. & Thomas, G. E. (1988). A Re-evaluation of Conventional Triaxial Test Methods, Advanced Triaxial Testing of Soil and Rock, ASTM STP 977, Philadelphia: ASTM, 219-263.

BS EN ISO 17892-2 (2014). Geotechnical investigation and testing. Laboratory testing of soil. Determination of bulk density. British Standards Document. https://doi.org/10.3403/30277799U.

Corti, R., Diambra, A., Wood, D. M., Escribano, D. E., & Nash, D. F. (2016). Memory surface hardening model for granular soils under repeated loading conditions. Journal of Engineering Mechanics, 142(12), 04016102.

Corti, R., Gourvenec, S. M., Randolph, M. F., & Diambra, A. (2017). Application of a memory surface model to predict whole-life settlements of a sliding foundation. Computers and Geotechnics, 88, 152-163.

Di Benedetto, H., Cazacliu, B., Geoffroy, H. & Sauzeat, C. (1999). Sand behaviour in very small to medium strain domains, Proc. of 2nd IS on Pre-failure Deformation Characteristics of Geomaterials, Torino: 89-96.

Doanh, T., Ibraim, E. & Matiotti, R. (1997). Undrained instability of very loose Hostun sand in triaxial compression and extension. Part 1: experimental observations. Mechanics of Cohesive-frictional Materials: An International Journal on Experiments, Modelling and Computation of Materials and Structures, Vol 2(1), 47-70.

Doanh, T., & Ibraim E. (2000). Minimum undrained strength of Hostun RF sand. Géotechnique, 50(4): 377-392.

Duttine, A., Di Benedetto, H., Van Bang, D. P. & Ezaoui, A. (2007). Anisotropic small strain elastic properties of sands and mixture of sand-clay measured by dynamic and static methods. Soils and foundations, 47(3): 457-472.

Escribano, D. E., Nash, D. F. T. & Diambra, A. (2018). Local and global volumetric strain comparison in sand specimens subjected to drained cyclic and monotonic triaxial compression loading. Geotechnical Testing Journal, 42 (4): 1006-1030. https://doi.org/10.1520/GTJ20170054.

Ezaoui, A. & Di Benedetto, H. (2009). Experimental measurements of the global anisotropic elastic behaviour of dry Hostun sand during triaxial tests, and effect of sample preparation. Géotechnique, 59(7): 621-635.

Hardin, B. O., & Blandford, G. E. (1989). Elasticity of particulate materials. Journal of Geotechnical Engineering, 115(6): 788-805.

Hight, D.W., Gens, A. & Symes, M. J. (1983). The development of a new hollow cylinder apparatus for investigating the effects of principal rotation in soils. Géotechnique 33(4): 355–383, https://doi.org/10.1680/geot.1983.33.4.355.

HongNam, N., & Koseki, J. (2005). Quasi-elastic deformation properties of Toyoura sand in cyclic triaxial and torsional loadings. Soils and foundations, 45(5), 19-37.

Hoque, E., & Tatsuoka, F. (1998). Anisotropy in elastic deformation of granular materials. Soils and Foundations, 38(1): 163-179.

Ibraim, E., Christiaens, P. & Pope, M. (2011). Development of a hollow cylinder torsional apparatus for pre-failure deformation and large strains behaviour of sand. Geotech. Engng J. of SEAGS & AGSSEA, Special Issue on Soil Behaviour 42(4): 58–68.

Ibraim, E., Diambra, A., Russell, A. R. & Wood, D. M. (2012). Assessment of laboratory sample preparation for fibre reinforced sands. Geotextiles and Geomembranes, 34: 69-79. doi:10.1016/j.geotexmem.2012.03.002.

Jardine, R.J., Symes, M.J. & Burland, J.B. (1984). The measurement of soil stiffness in the triaxial apparatus. Géotechnique, 34(3), 323-340.

Liu, H., Abell, J. A., Diambra, A. & Pisanò, F. (2018). Modelling the cyclic ratcheting of sands through memory-enhanced bounding surface plasticity. Géotechnique, 69(9): 783-800.

Mandolini, A., Diambra, A. & Ibraim, E. (2019). Strength anisotropy of fibre-reinforced sands under multiaxial loading. Géotechnique, 69(3): 203-216. https://doi.org/10.1680/jgeot.17.P.102.

Mandolini, A., 2018. Change in elastic properties of sands under very large number of low amplitude multiaxial cyclic loading. PhD Thesis. Department of Civil Engineering, University of Bristol (UK).

Matsuoka, H. & Nakai, T. (1974). Stress-deformation and strength characteristics of soil under three different principal stresses. In Proceedings of the Japan Society of Civil Engineers Vol 1974, No. 232: 59-70.

Miura, K., Miura, S. & Toki, S. (1986). Deformation behavior of anisotropic dense sand under principal stress axes rotation. Soils and Foundations, 26 (1):36–52.

Randolph, M.F. & Gourvenec, S.M. (2010). Offshore Geotechnical Engineering. Taylor &Francis, London, ISBN: 978-0-415-47744-4.

Roesler, S. K. (1979). Anisotropic shear modulus due to stress anisotropy. Journal of the Geotechnical Engineering Division, 105(7): 871-880.

Shibuya S., Tatsuoka F., Teachavorasinskun S., Kong, X.J., Abe, F., Kim, Y-S., Park, C-S. (1992). Elastic deformation properties of geomaterials, Soils and Foundations, 32(3): 26-46.

Tatsuoka, F., Sonoda, S., Hara, K., Fukushima, S. & Pradhan, T. B. S. (1986). Failure and deformation of sand in torsional shear. Soils and Foundations, 26(4):79–97.

Tatsuoka, F., Sato, T., Park, C.- S., Kim, Y.- S., Mukabi, J. N., and Kohata, Y. (1994) Measurement of Elastic Properties of Geomaterials in Laboratory Compression Tests. Geotechnical Testing Journal, 17 (1): 80–94.

Tong, Z. X., Zhang, J. M., Yu, Y. L., & Zhang, G. (2010). Drained deformation behavior of anisotropic sands during cyclic rotation of principal stress axes. Journal of Geotechnical and Geoenvironmental Engineering, 136(11): 1509-1518.

Vaid, Y.P., Sayao, A., Hou, E. & Negussey, D. (1990). Generalized stress-path-dependent soil behaviour with a new hollow cylinder torsional apparatus. Canadian Geotechnical Journal, 27(5): 601–616. Available at: https://doi.org/10.1139/t90-075.

Wichtmann, T., & Triantafyllidis, T. (2004a). Influence of a cyclic and dynamic loading history on dynamic properties of dry sand, part II: cyclic axial preloading. Soil Dynamics and Earthquake Engineering, 24(11): 789-803.

Wichtmann, T., & Triantafyllidis, T. (2004b). Influence of a cyclic and dynamic loading history on dynamic properties of dry sand, part I: cyclic and dynamic torsional prestraining. Soil Dynamics and Earthquake Engineering, 24(2): 127-147.

Wichtmann, T., Niemunis, A., & Triantafyllidis, T. (2005). Strain accumulation in sand due to cyclic loading: drained triaxial tests. Soil Dynamics and Earthquake Engineering, 25(12): 967-979.

Wichtmann, T., Niemunis, A., & Triantafyllidis, T. (2007a). Strain accumulation in sand due to cyclic loading: drained cyclic tests with triaxial extension. Soil Dynamics and Earthquake Engineering, 27(1): 42-48.

Wichtmann, T., Niemunis, A., & Triantafyllidis, T. (2007b). On the influence of the polarization and the shape of the strain loop on strain accumulation in sand under high-cyclic loading. Soil Dynamics and Earthquake Engineering, 27(1): .14-28.

Notation list

C	coefficient for Young's modulus dependency on void ratio and pressure
D	coefficient for shear modulus dependency on void ratio and pressure
C_g	coefficient of gradation (=$(D_{30})^2/(D_{60}\,D_{10})$)
C_u	coefficient of uniformity (=D_{60}/D_{10})
D_{10}, D_{30}, D_{60}	particle size such that 10, 30 and 60% of the particles are smaller than D_{10}, D_{30} and D_{60}
D_{50}	mean grain size
D_E	normalised variation of vertical Young's modulus
D_G	normalised variation of shear modulus
E_z	vertical Young's modulus
$E_{z(i)}$	vertical Young's modulus at the start of each cyclic loading stage
$E_{z(f)}$	vertical Young's modulus at the end of each cyclic loading stage
$G_{\vartheta z}$	shear modulus
$G_{\vartheta z(i)}$	shear modulus at the start of each cyclic loading stage
$G_{\vartheta z(f)}$	shear modulus at the end of each cyclic loading stage
e	void ratio
e_{min}, e_{max}	minimum and maximum void ratio
$f(e)$	void ratio function
H	height of HCTA sample
m	exponent for pressure dependency of vertical Young's modulus
n_1, n_2	exponents for pressure dependency of shear modulus
Po	inner pressure in HCTA test
Pi	outer pressure in HCTA test
p'	mean effective stress
q	deviator stress
r_o	inner radius HCTA sample
r_i	outer radius HCTA sample
α_σ	orientation of major principal stress axis
β	relative orientation between cyclic loading and monotonic stress path
ε_z	axial strain
ε_r	radial strain
ε_ϑ	circumferential strain
ϕ'_m	mobilised friction angle
$\gamma_{\vartheta z}$	torsional strain
$\Delta\alpha_{cyc}$	re-orientation of principal stress axis during cyclic loading
$\Delta\varepsilon_z$	variation in axial strain
$\Delta\gamma_{\vartheta z}$	variation in shear strain
$\Delta\sigma_z$	variation in axial stress
$\Delta\tau_{\vartheta z}$	variation in shear stress
σ_1, σ_2, σ_3	major, intermediate and minor principal stress
σ_{ref}	reference pressure = 1 kPa
σ_ϑ	circumferential stress
σ_r	radial stress
σ_z	axial stress
$\tau_{\vartheta z}$	torsional stress

List of tables and figures

Table 1 List and details of type I tests performed in this experimental investigation

Test Name	Pre-cyclic stress state			Cyclic loading characteristics (axial or shear) at different test stages†					Stiffness at investigation point (before (i) and at the end (f) of the cyclic loading) ††			
	$(\sigma'_z-\sigma'_\vartheta)/(2p')$	$\tau_{\vartheta z}/p'$	e	Stage	$\Delta\sigma'_z$	$\Delta\tau_{\vartheta z}$	$\Delta\alpha_{cyc}$	Cycles	$E_{z(i)}$	$E_{z(f)}$	$G_{\vartheta z(i)}$	$G_{\vartheta z(f)}$
				No.	(kPa)	(kPa)	(°).	No.	(MPa)	(MPa)	(MPa)	(MPa)
A-β0	0.400	-	0.815	c1	±5	-	0	3240	257.7	258.8	83.1	83.5
	0.711	-	0.815	c2	±5	-	0	2880	336.7	332.9	94.5	93.5
	0.400	-	0.815	c3	±5	-	0	3240	264.1	257.3	85.2	83.0
	-0.333	-	0.816	c4	±5	-	0	3240	107.0	102.1	54.9	53.0
	0.401	-	0.814	c5	±5	-	0	12240	250.0	244.7	80.7	78.9
	0.000	-	0.815	c6	±5	-	0	3240	184.7	176.0	59.6	56.9
							TOT	**28080**				
A-β90	0.406	-	0.823	c1	-	±5	±3.0	3240	240.2	241.3	76.5	76.8
	0.713	-	0.823	c2	-	±5	±1.5	6480	326.9	330.4	91.8	92.8
	0.404	-	0.823	c3	-	±5	±3.1	3780	240.5	237.5	72.0	70.2
	-0.320	-	0.823	c4	-	±5	±4.9	3420	95.0	96.0	55.7	51.1
	0.406	-	0.820	c5	-	±5	±3.0	3330	221.3	223.0	76.9	76.1
	-0.001	-	0.821	c6	-	±5	-	16380	164.5	159.5	66.2	66.1
							TOT	**36630**				
T-β0	-	0.368	0.826	c1	-	±5	0	3240	148.6	149.7	60.7	59.9
	-	0.505	0.826	c2	-	±5	0	3240	133.7	136.4	48.9	52.0
	-	0.337	0.826	c3	-	±5	0	3240	145.9	143.8	57.5	55.7
	-	-0.420	0.822	c4	-	±5	0	3240	130.6	132.6	54.5	54.6
	-	0.370	0.820	c5	-	±5	0	3240	142.8	144.6	56.5	53.1
	-	0.009	0.819	c6	-	±5	0	3240	147.6	146.2	59.9	59.5
							TOT	**19440**				
T-β90	-	0.337	0.833	c1	±5	-	±4.2	3780	169.0	168.2	64.5	64.0
	-	0.511	0.833	c2	±5	-	±2.9	3240	140.0	142.8	55.8	54.1
	-	0.344	0.833	c3	±5	-	±4.2	3240	162.2	161.5	61.3	60.3
	-	-0.208	0.830	c4	±5	-	±6.9	3240	149.9	157.5	58.3	61.9
	-	0.344	0.829	c5	±5	-	±4.2	3240	161.4	158.8	59.8	59.6
	-	-0.047	0.829	c6	±5	-	-	3420	167.3	162.6	65.4	65.2
							TOT	**20160**				

†The frequency of all cyclic loading stages was 0.05Hz; †† The frequency of cycles employed for the small strain stiffness investigation was 0.005Hz.

Table 1 List and details of type II tests performed in this experimental investigation

Test Name	Pre-cyclic stress state			Cyclic loading characteristics (axial or shear) at different test stages†					Stiffness at investigation point (before (i) and at the end (f) of the cyclic loading) ††			
	$(\sigma'_z-\sigma'_\vartheta)/(2p')$	$\tau_{\vartheta z}/p'$	e	Stage	$\Delta\sigma'_z$	$\Delta\tau_{\vartheta z}$	$\Delta\alpha_{cyc}$	Cycles	$E_{z(i)}$	$E_{z(f)}$	$G_{\vartheta z(i)}$	$G_{\vartheta z(f)}$
				No.	(kPa)	(kPa)	(°)	No.	(MPa)	(MPa)	(MPa)	(MPa)
A-β90(L1)	0.397	-	0.824	c1	-	±3.3	±2.1	79200	227.7	218.0	75.3	74.6
	0.394	-	0.827	c2	-	±3.3	±2.1	95760	226.7	220.6	71.7	70.2
							TOT	**174960**				
A-β90(L2)	0.716	-	0.821	c1	-	±3	±0.9	23670	292.0	287.1	79.2	78.7
	0.717	-	0.820	c2	-	±3	±0.9	11970	297.7	294.2	84.5	81.5
	0.717	-	0.819	c3	-	±3	±0.9	24210	300.6	298.6	84.8	81.7
	0.722	-	0.817	c4	-	±5	±1.5	60570	304.4	293.7	84.8	79.7
	0.722	-	0.817	c5	-	±5	±1.5	11250	305.3	295.8	88.6	84.4
							TOT	**131670**				
A-β90β0	0.407	-	0.814	c1	-	±12	±7.1	27900	269.2	249.9	83.9	70.9
	0.406	-	0.814	c2	-	±12	±7.2	76949	267.1	238.2	83.8	71.7
	0.392	-	0.814	c3	-	±12	±7.4	46260	253.3	239.0	84.7	69.8
	0.392	-	0.814	c4	-	±12	±7.5	8145	259.0	241.6	86.6	72.4
	0.392	-	0.813	c5	-	±12	±7.4	58860	253.7	231.8	86.6	72.4
	0.392	-	0.812	c6	-	±12	±7.4	43740	252.2	242.1	85.9	69.2
	0.393	-	0.811	c7	-	±12	±7.4	28530	255.6	240.5	87.0	71.2
	0.393	-	0.811	c8	-	±5	±3.2	23130	263.6	251.9	88.1	77.0
	0.391	-	0.811	c9	±5	-	0	47250	271.2	262.9	89.7	88.4
	0.393	-	0.811	c10	-	±2	±1.3	69660	271.9	262.8	89.8	88.2
	0.393	-	0.810	c11	±5	-	0	12330	281.3	281.3	90.8	90.8
	0.393	-	0.811	c12	±5	-	0	8460	277.3	270.8	92.2	88.6
	0.393	-	0.811	c13	±5	-	0	15750	280.6	274.1	91.2	88.8
	0.393	-	0.811	c14	±5	-	0	81810	281.3	270.3	91.4	89.5
	0.393	-	0.811	c15	-	±5	±3.2	16740	283.9	270.4	93.0	87.1
	0.394	-	0.810	c16	-	±5	±3.2	39420	281.5	269.8	93.3	83.0
							TOT	**604935**				
T-β*	-	0.351	0.830	c1	±5	±5	-1.8; 2.4	71190	207.6	187.3	62.8	50.9
	-	0.390	0.830	c2	±5	±5	-1.6; 2.1	28800	187.6	172.6	57.8	49.4
	-	0.356	0.829	c3	±5	±5	-2.3; 1.8	8280	196.1	181.4	62.7	57.2
	-	0.351	0.828	c4	±5	±5	-2.4; 1.8	7920	203.9	188.0	63.3	57.4
	-	0.361	0.827	c5	±5	±5	-2.3; 1.7	37980	205.0	181.2	64.1	51.7
							TOT	**154170**				

†The frequency of all cyclic loading stages was 0.05Hz; †† The frequency of cycles employed for the small strain stiffness investigation was 0.005Hz.

Figure 1

Click here to access/download;Figure;Figure 1.tif

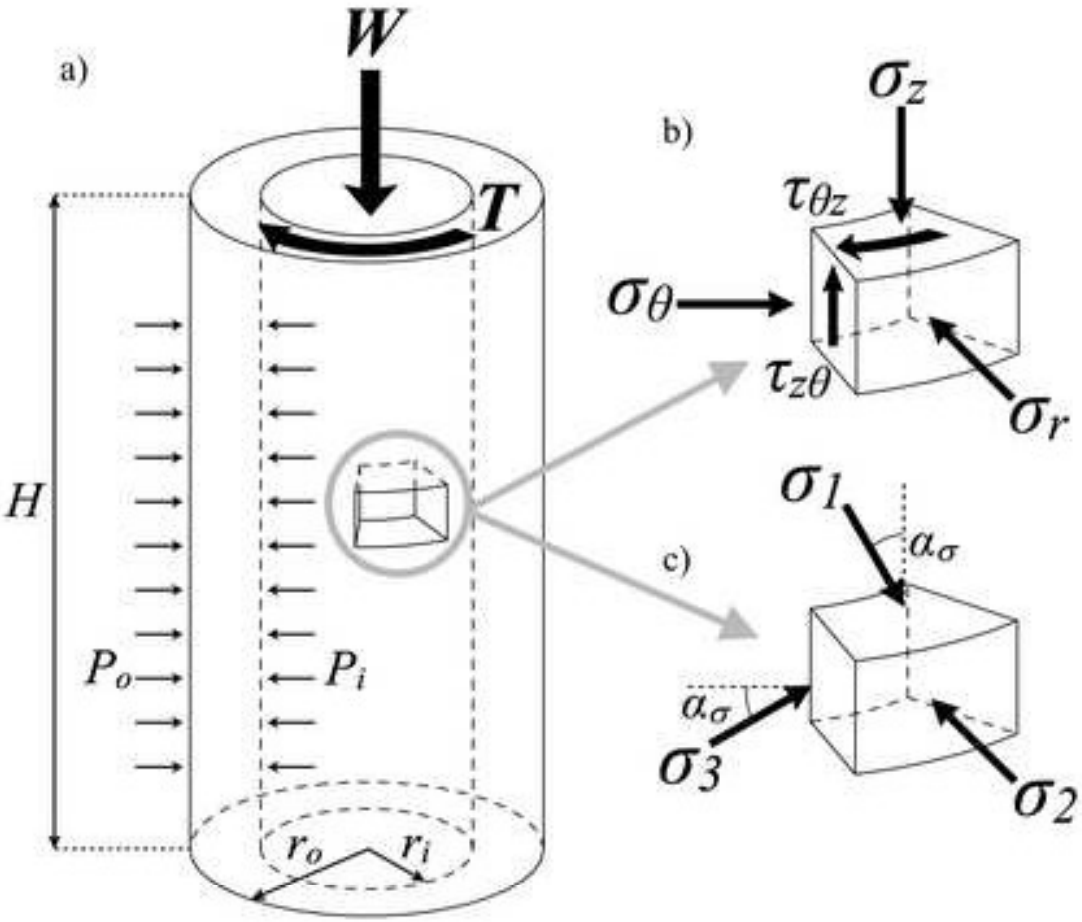

Figure 2

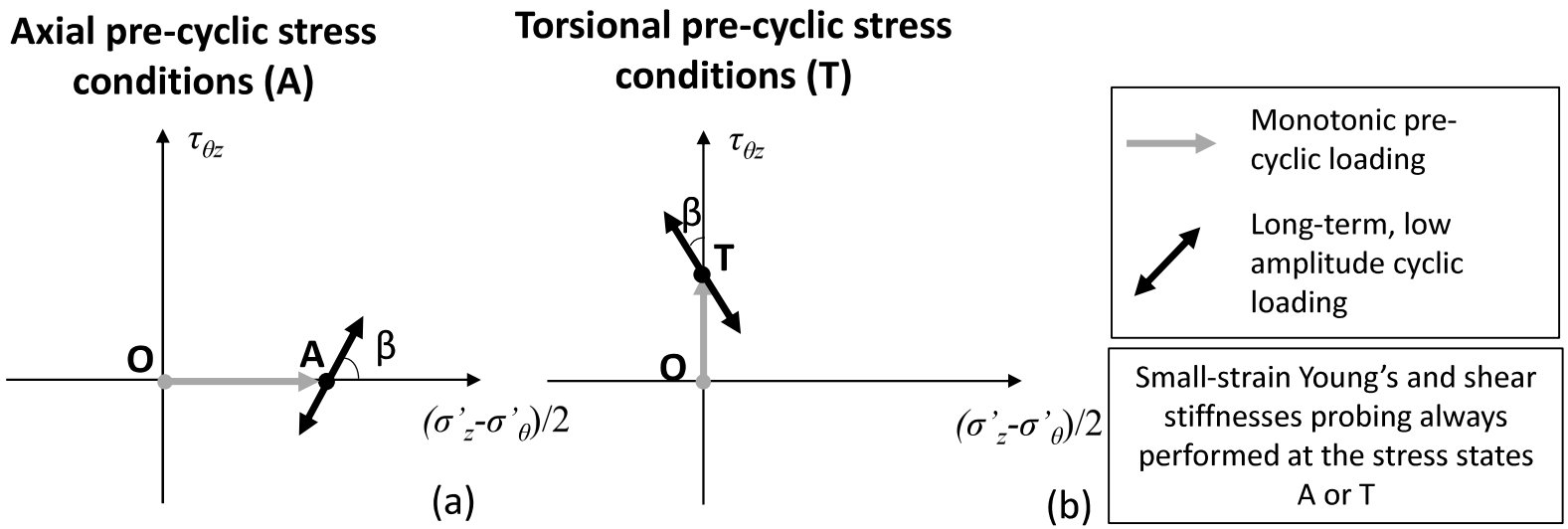

Figure 3

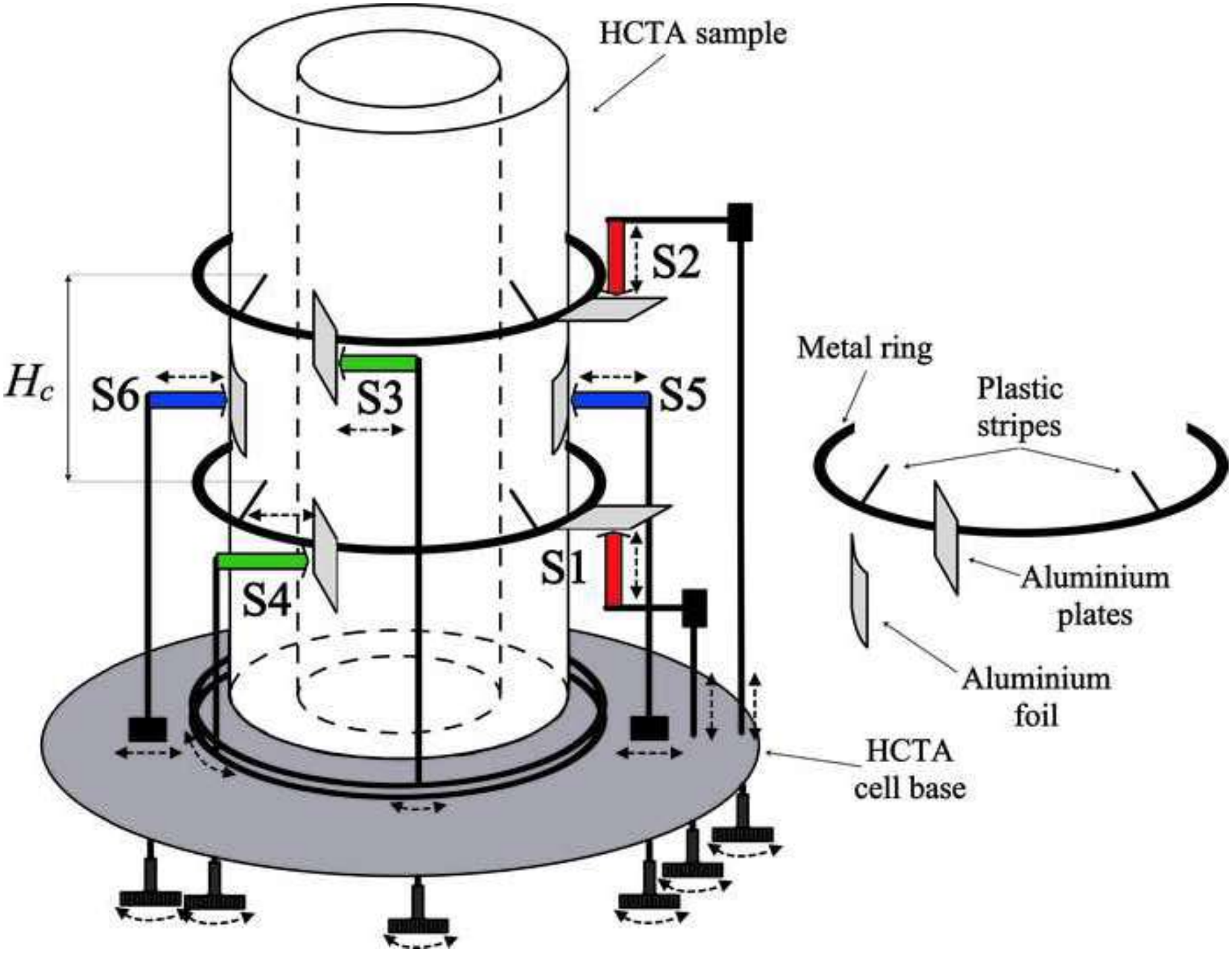

Figure 4ab

Click here to access/download;Figure;Figure 4 a, b.tif

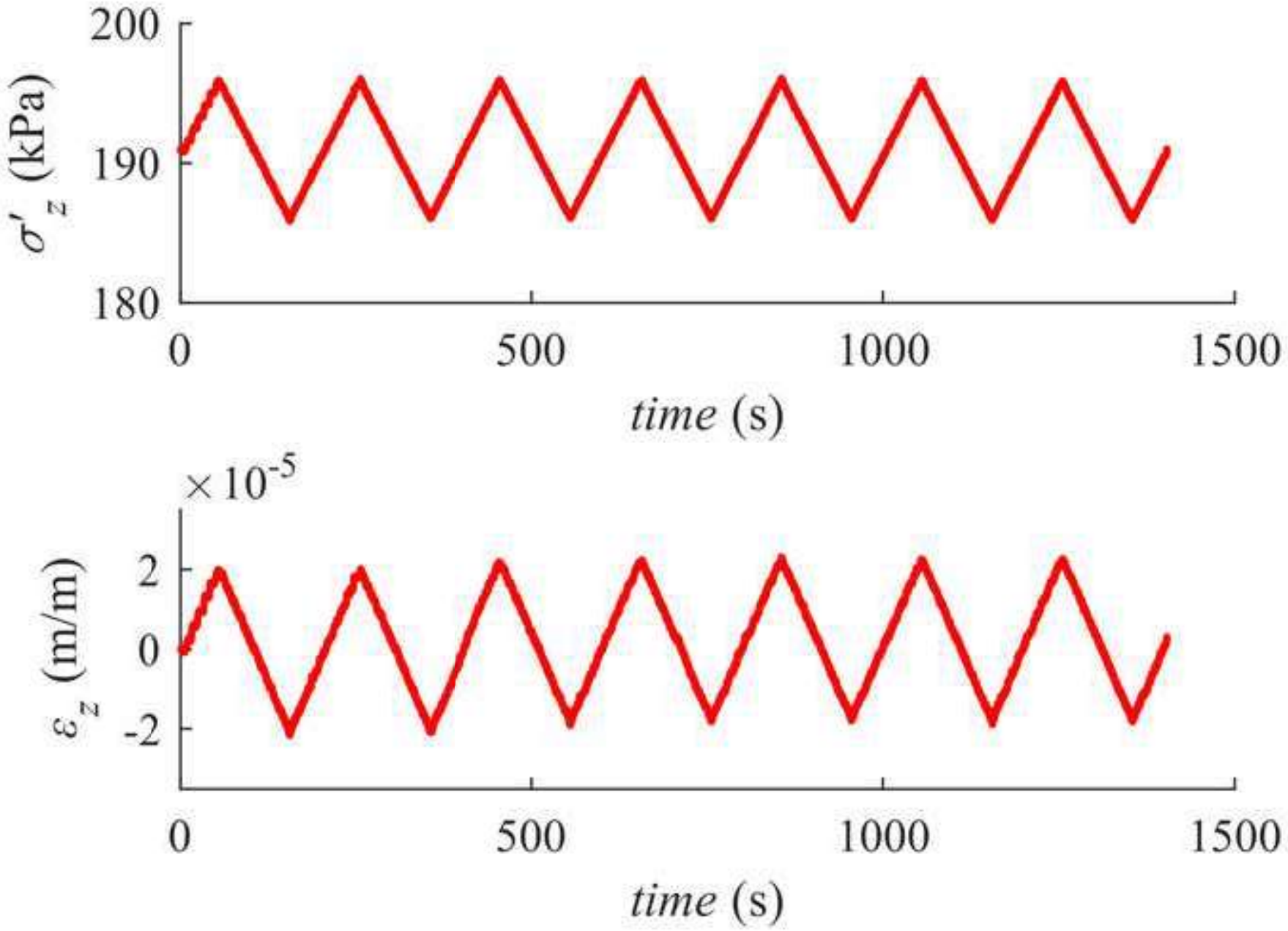

Figure 4c

Click here to access/download;Figure;Figure 4 c.tif

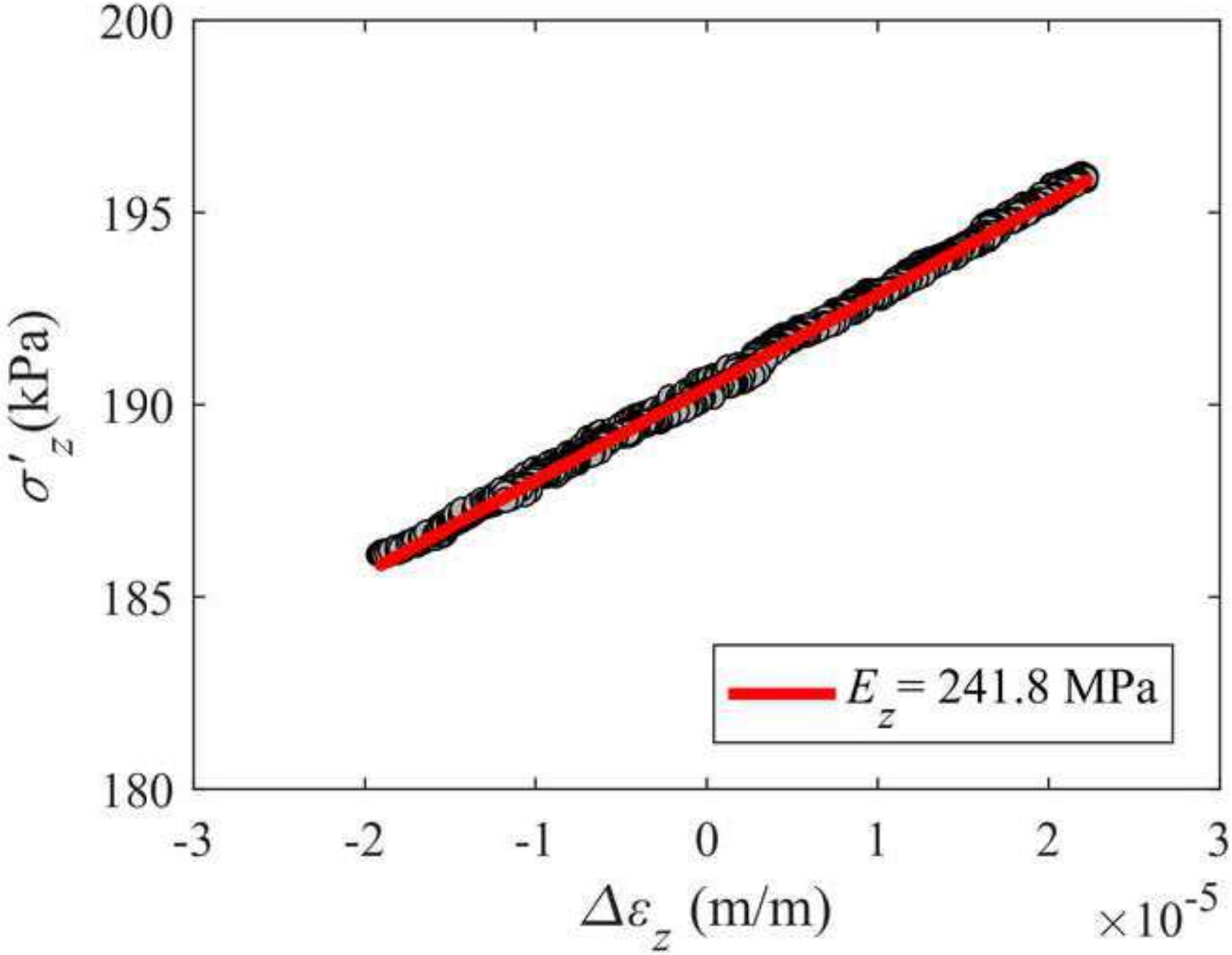

Figure 4de

Click here to access/download;Figure;Figure 4 d, e.tif

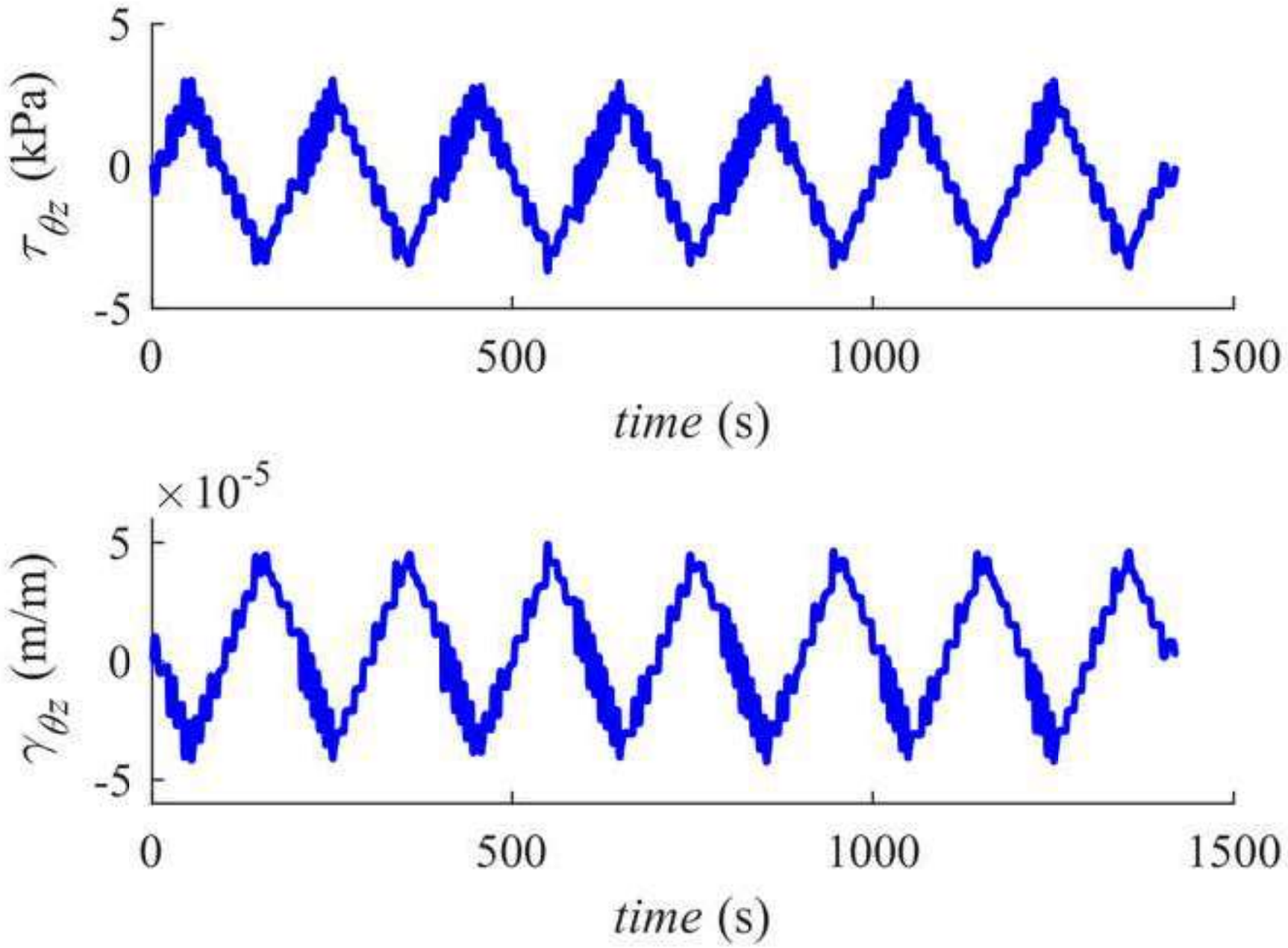

Figure 4f

Click here to access/download;Figure;Figure 4 f.tif

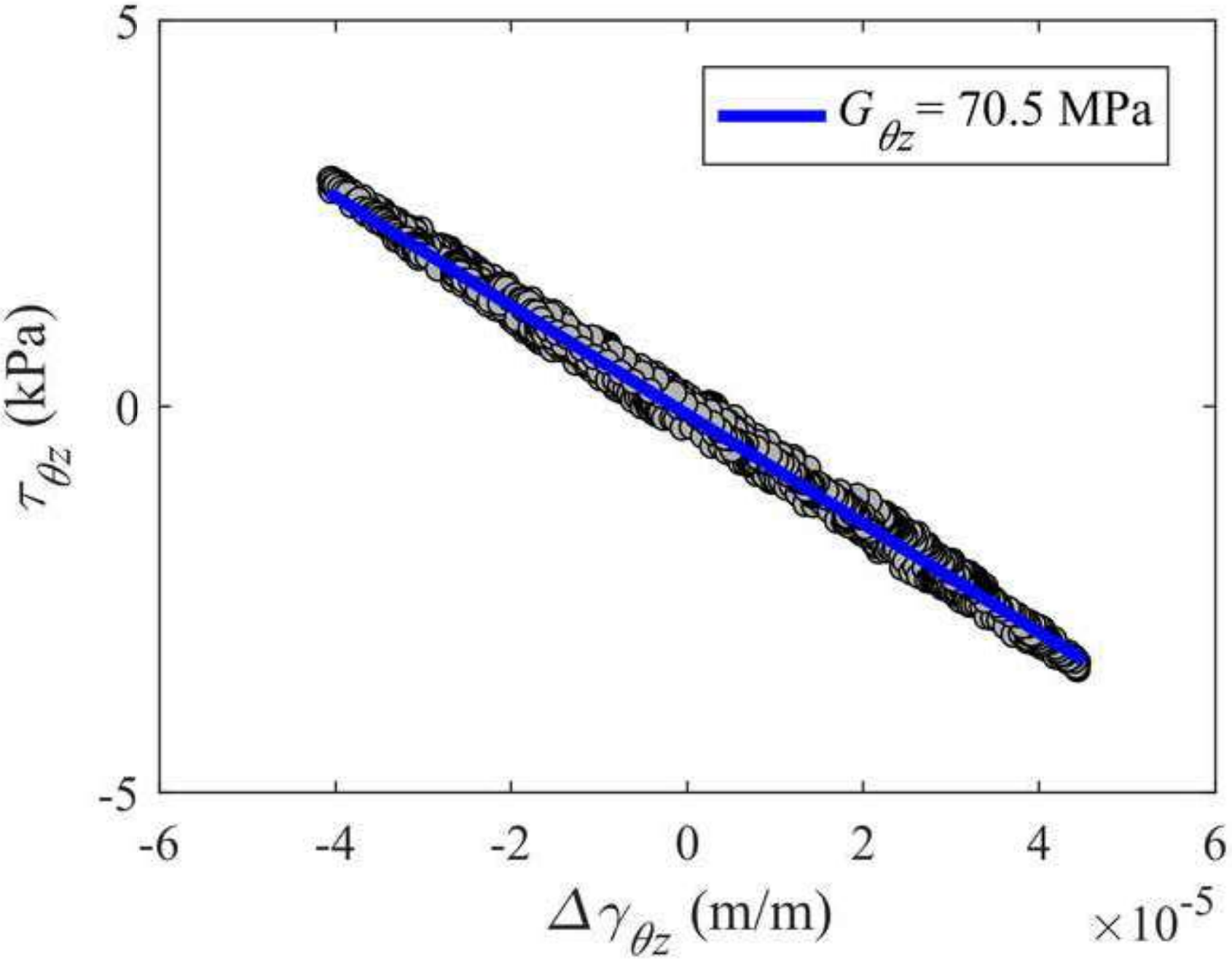

Figure 5

Click here to access/download;Figure;Figure 5v2.pptx

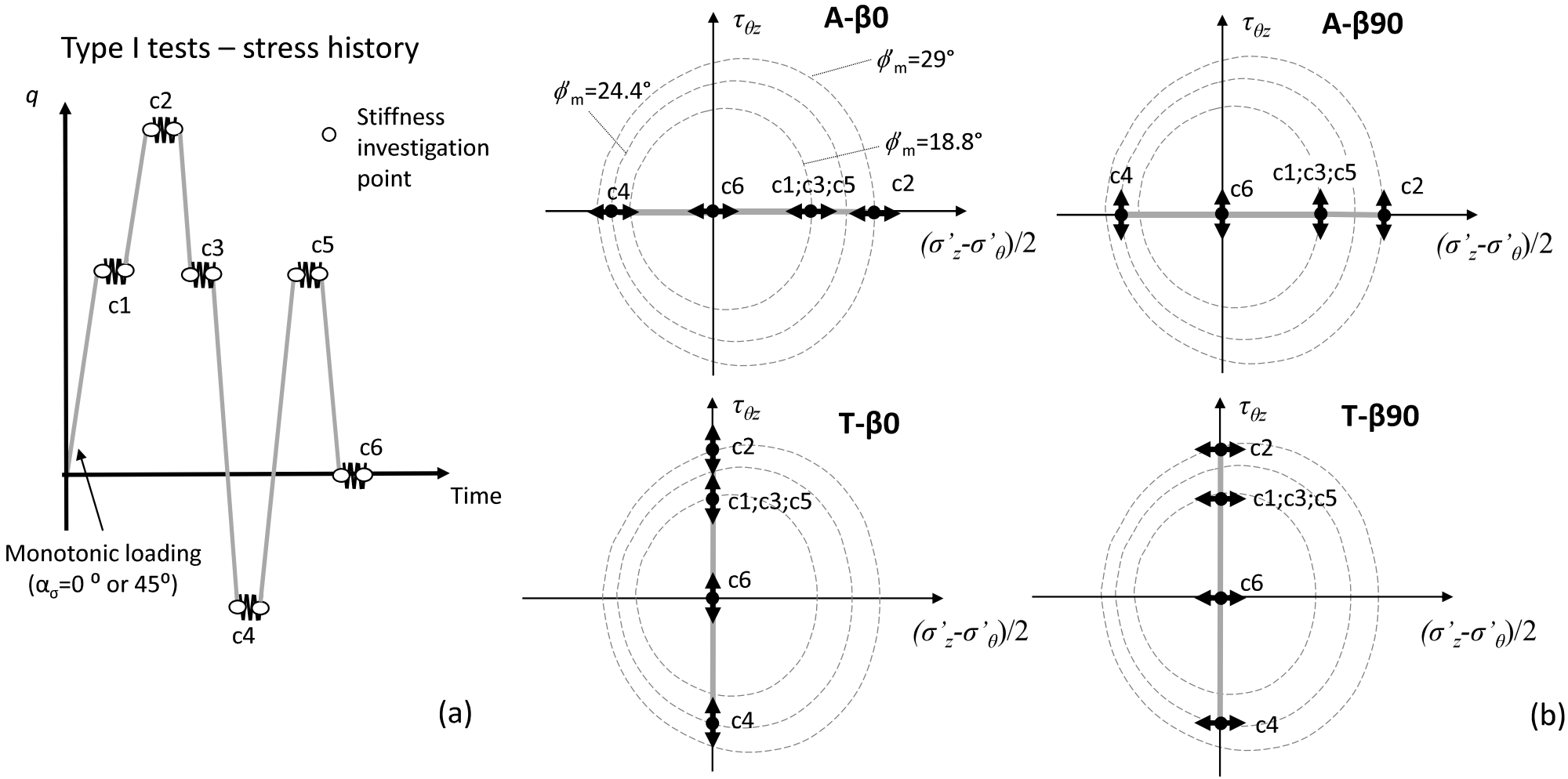

Figure 6

Click here to access/download;Figure;Figure 6v2.pptx

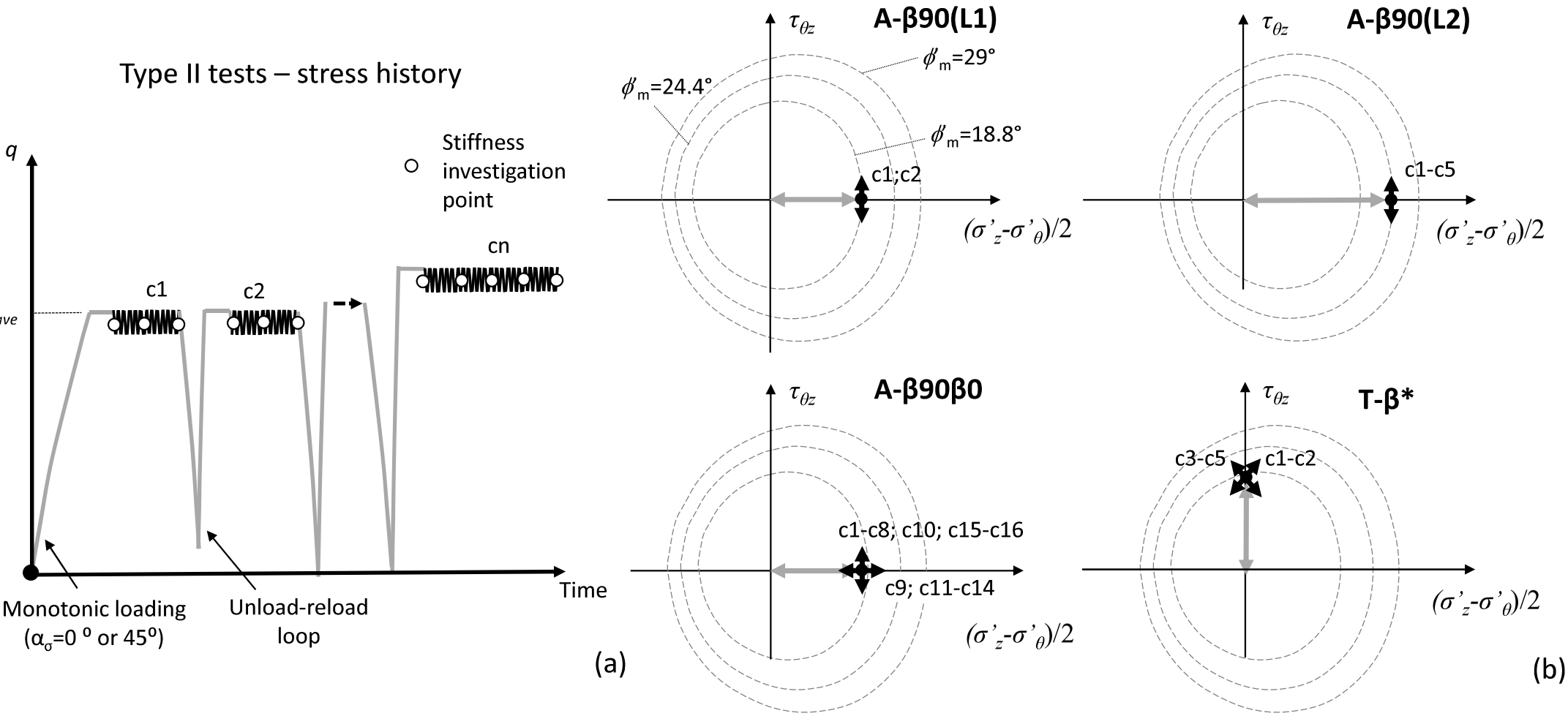

Figure 7a

Click here to access/download;Figure;Figure 7av2.tif

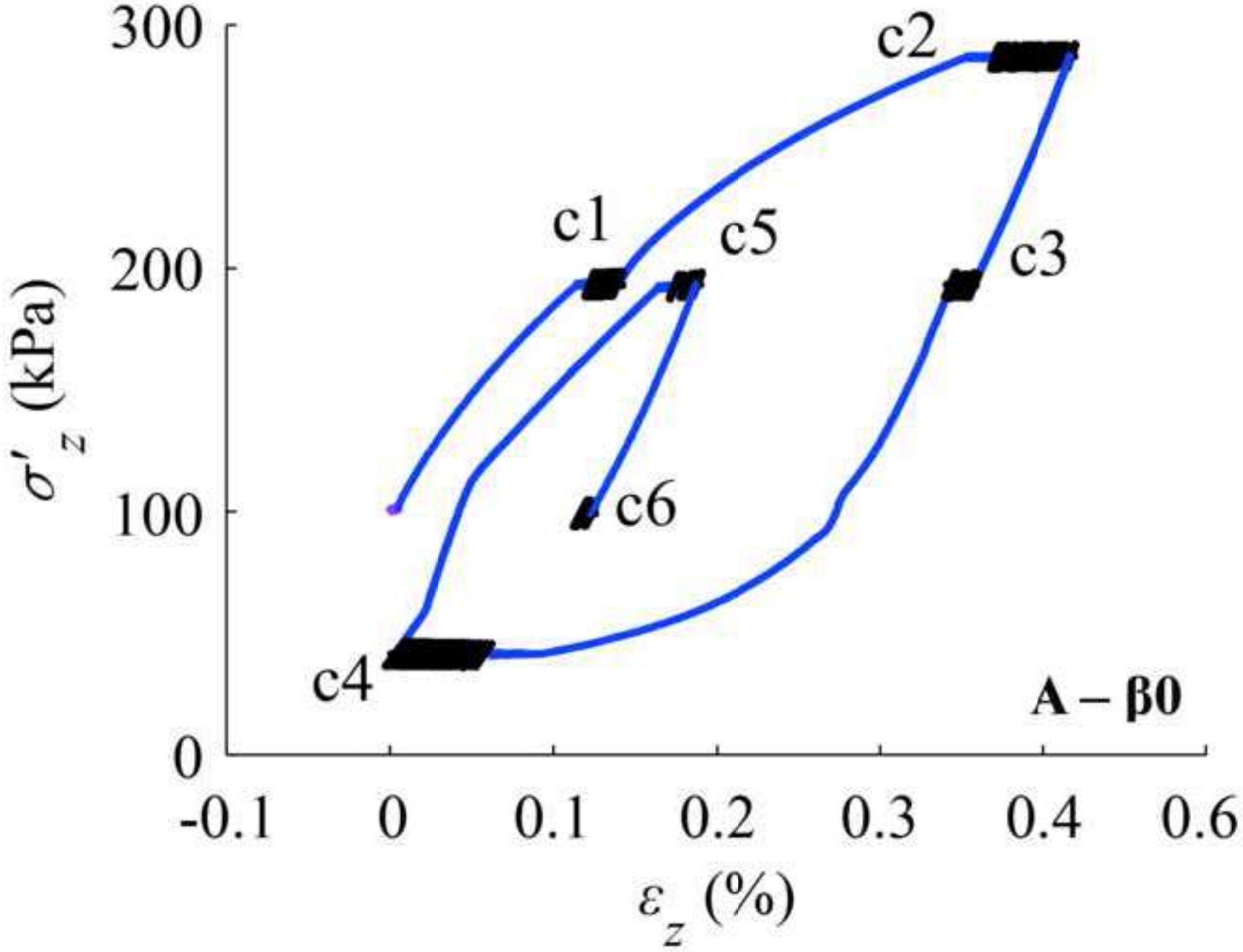

Figure 7b

Click here to access/download;Figure;Figure 7bv2.tif

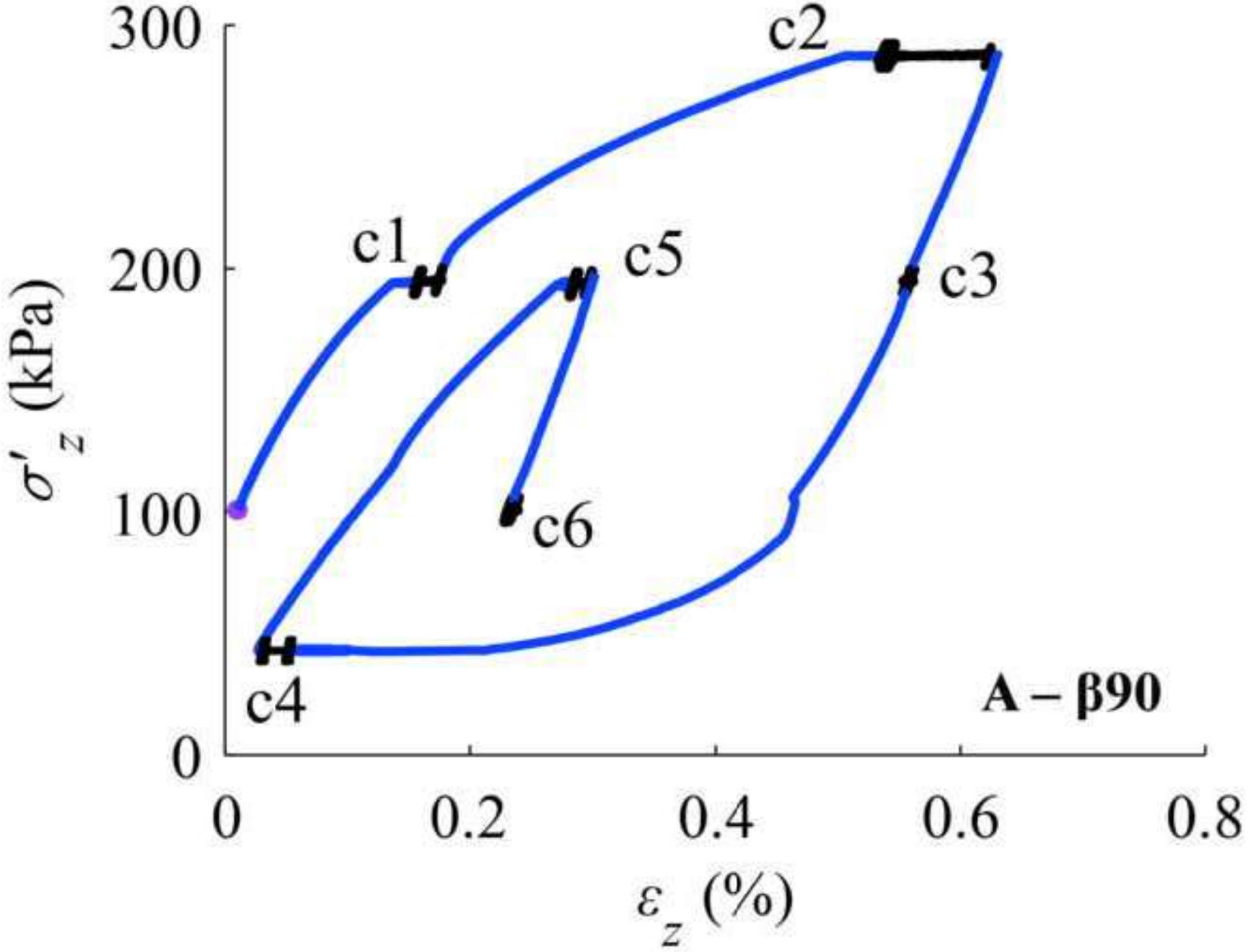

Figure 7c

Click here to access/download;Figure;Figure 7cv2.tif

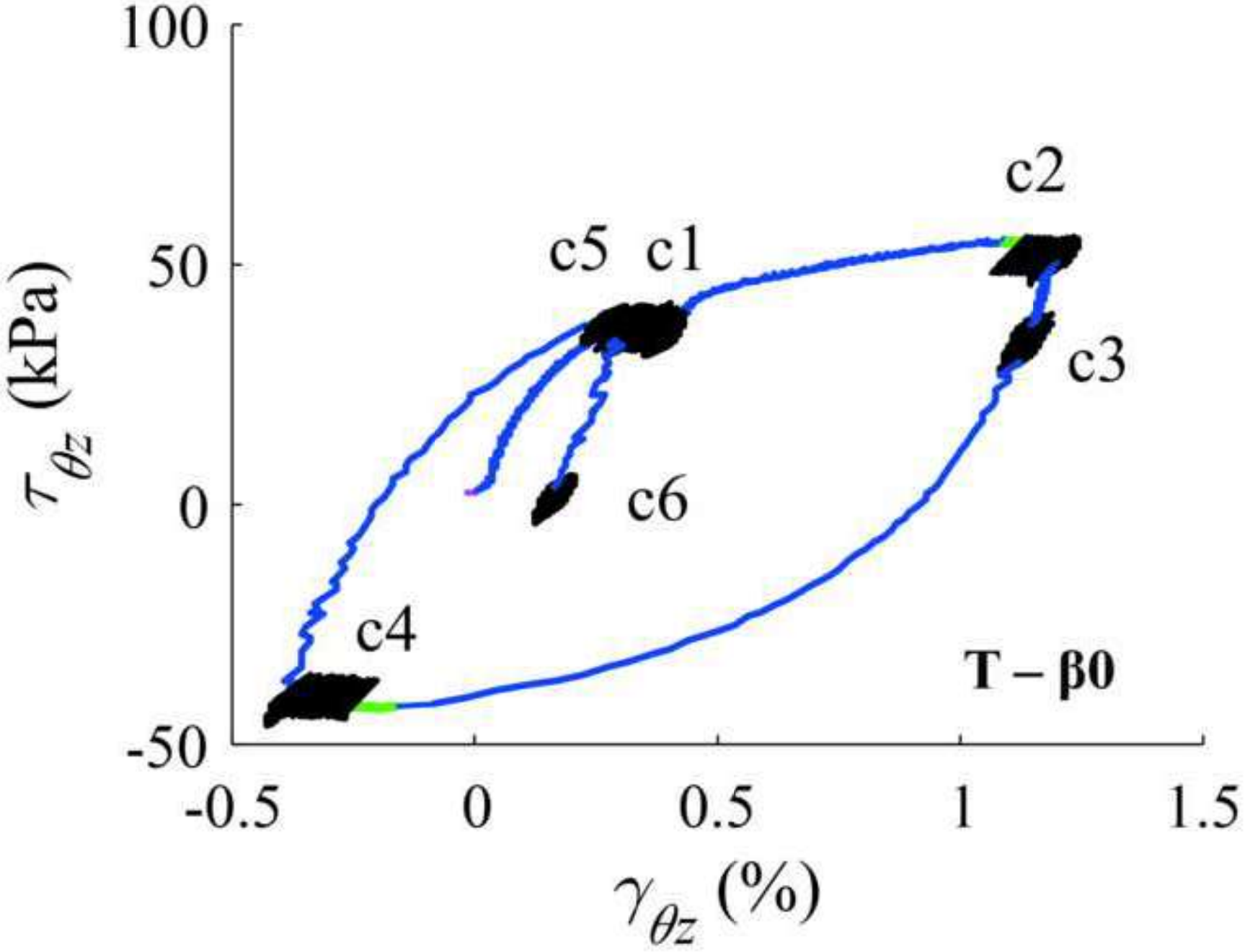

Figure 7d

Click here to access/download;Figure;Figure 7dv2.tif

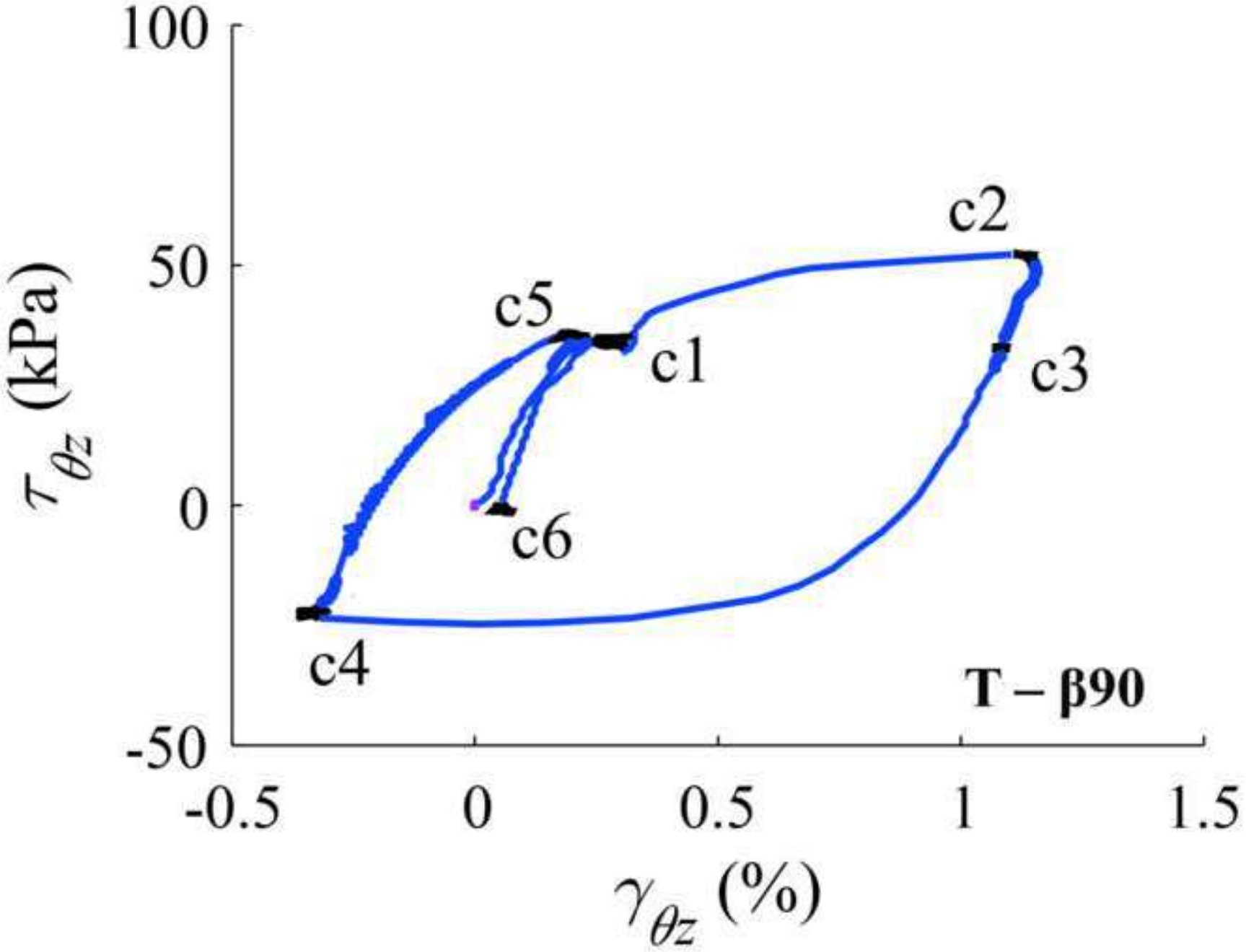

Figure 8

Click here to access/download;Figure;Figure 8.tif

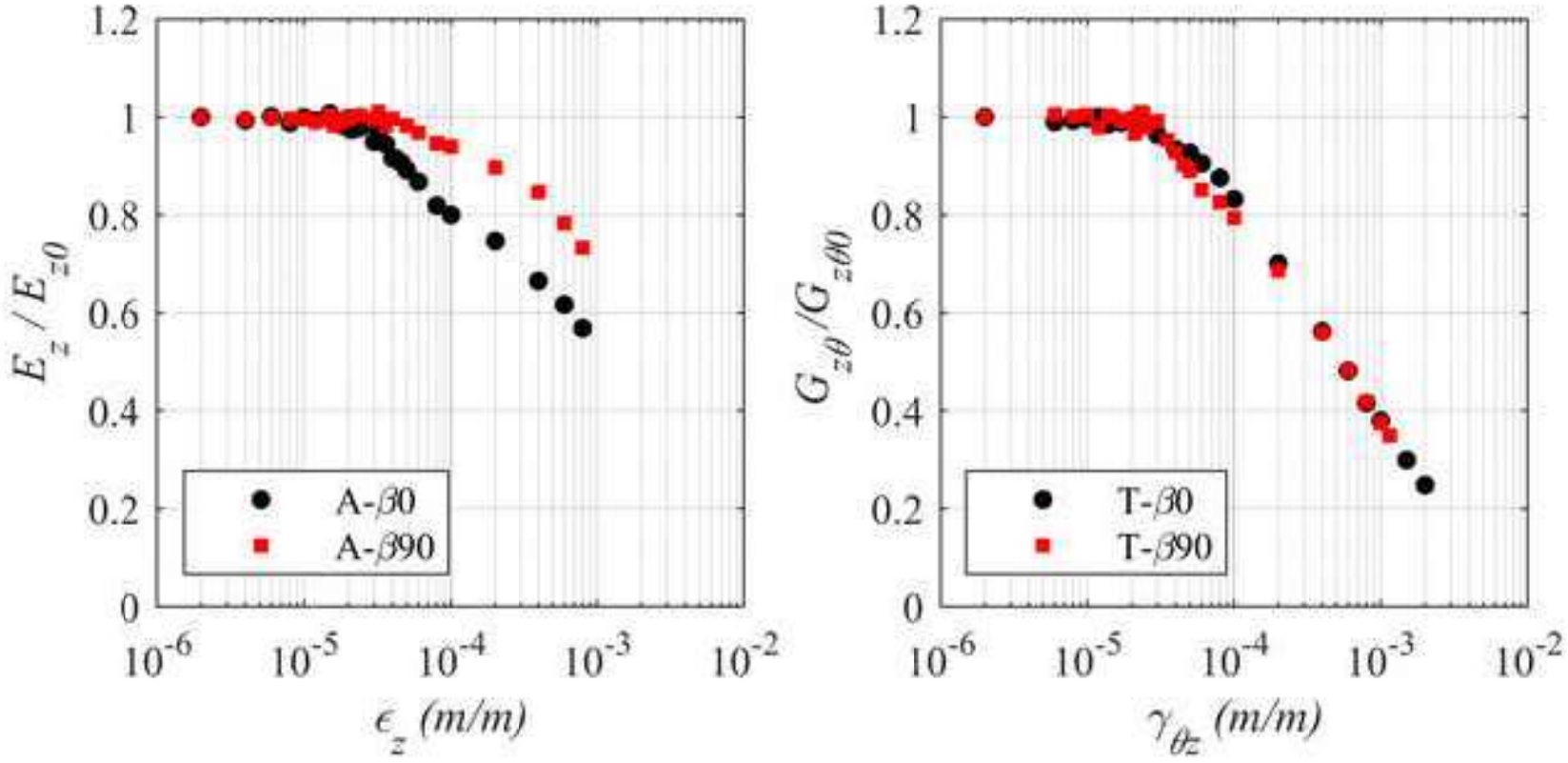

Figure 9

Click here to access/download;Figure;Figure 9.tif

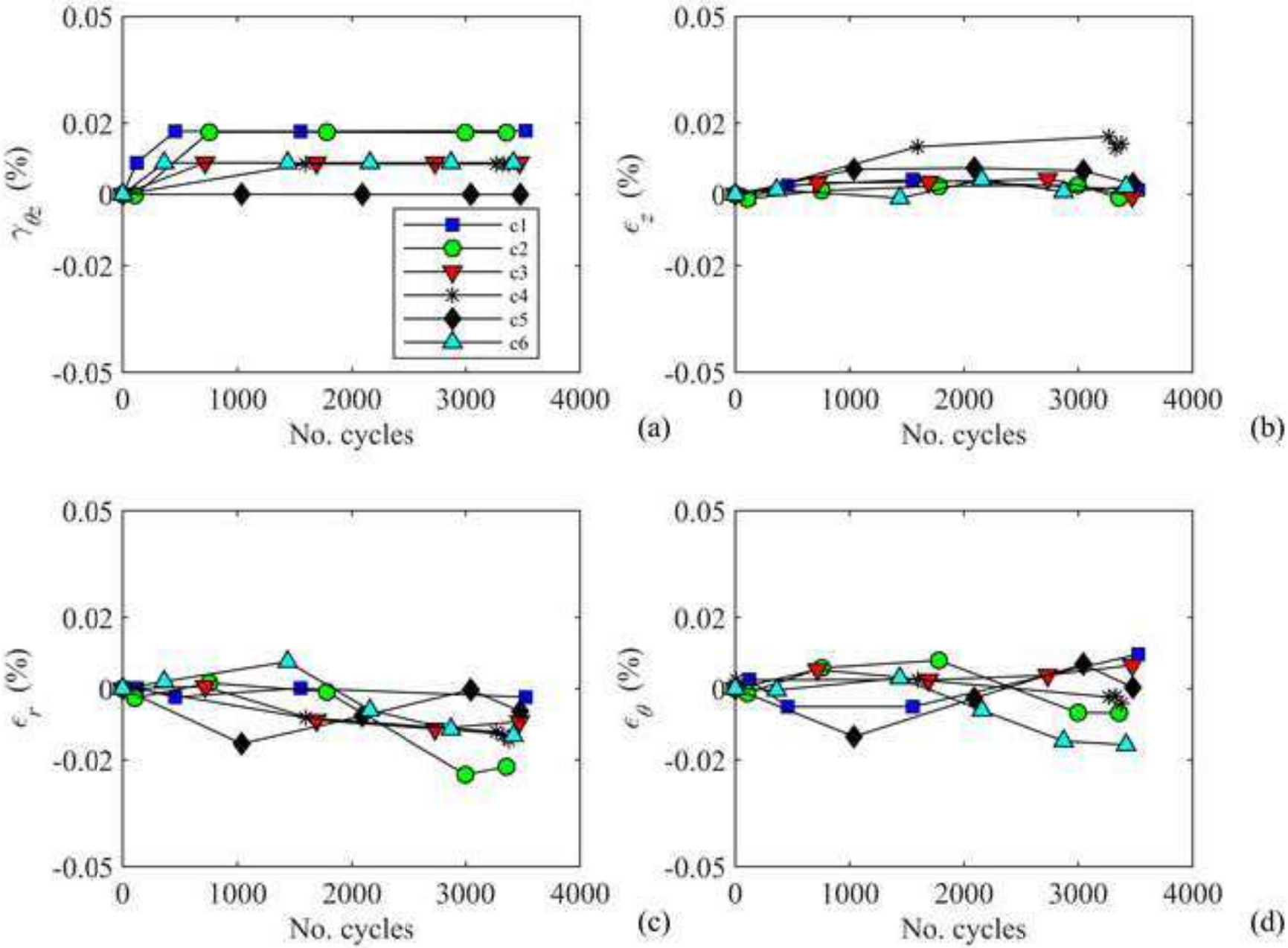

Figure 10

Click here to access/download;Figure;Figure 10.tif

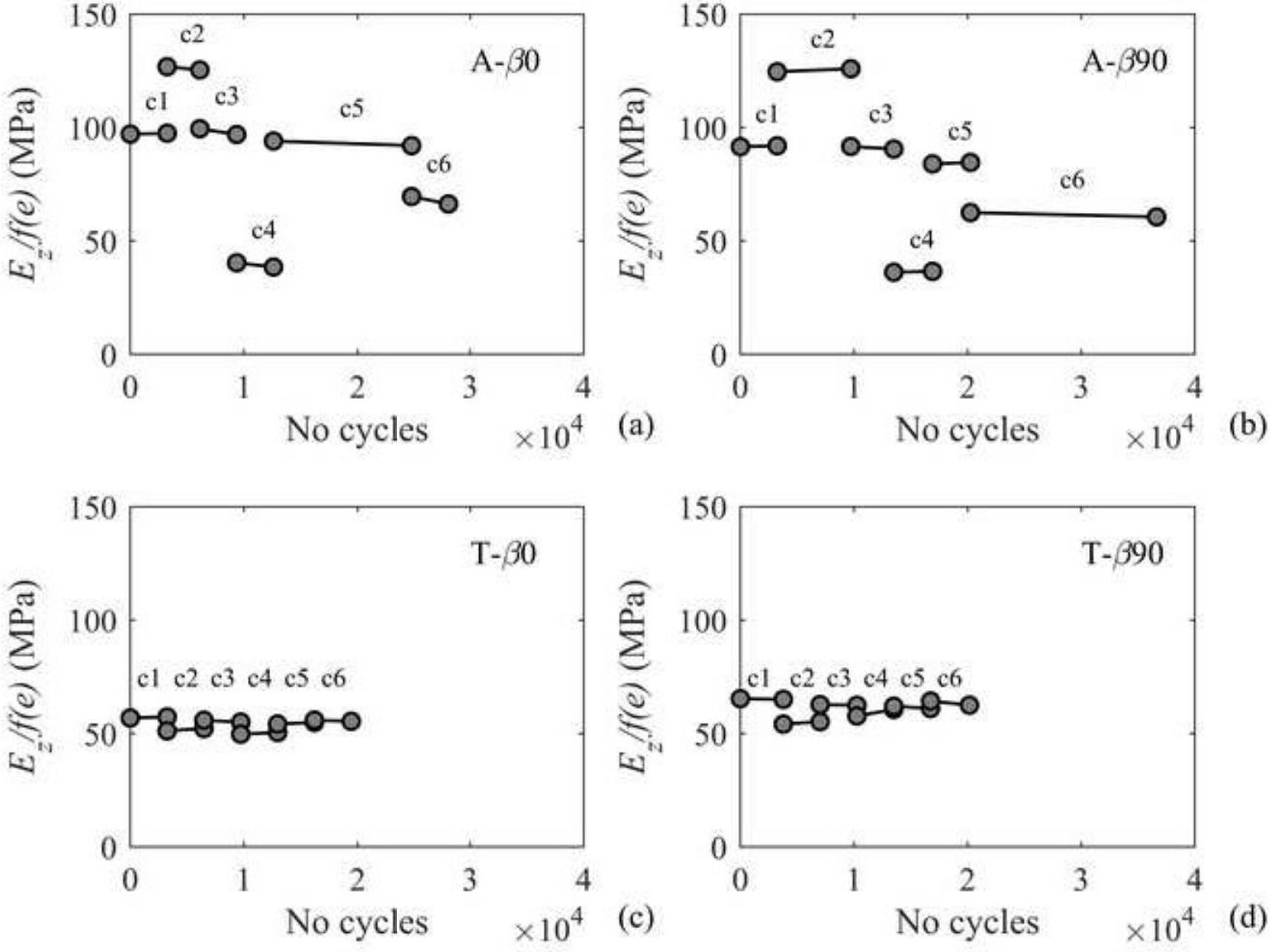

Figure 11

Click here to access/download;Figure;Figure 11.tif

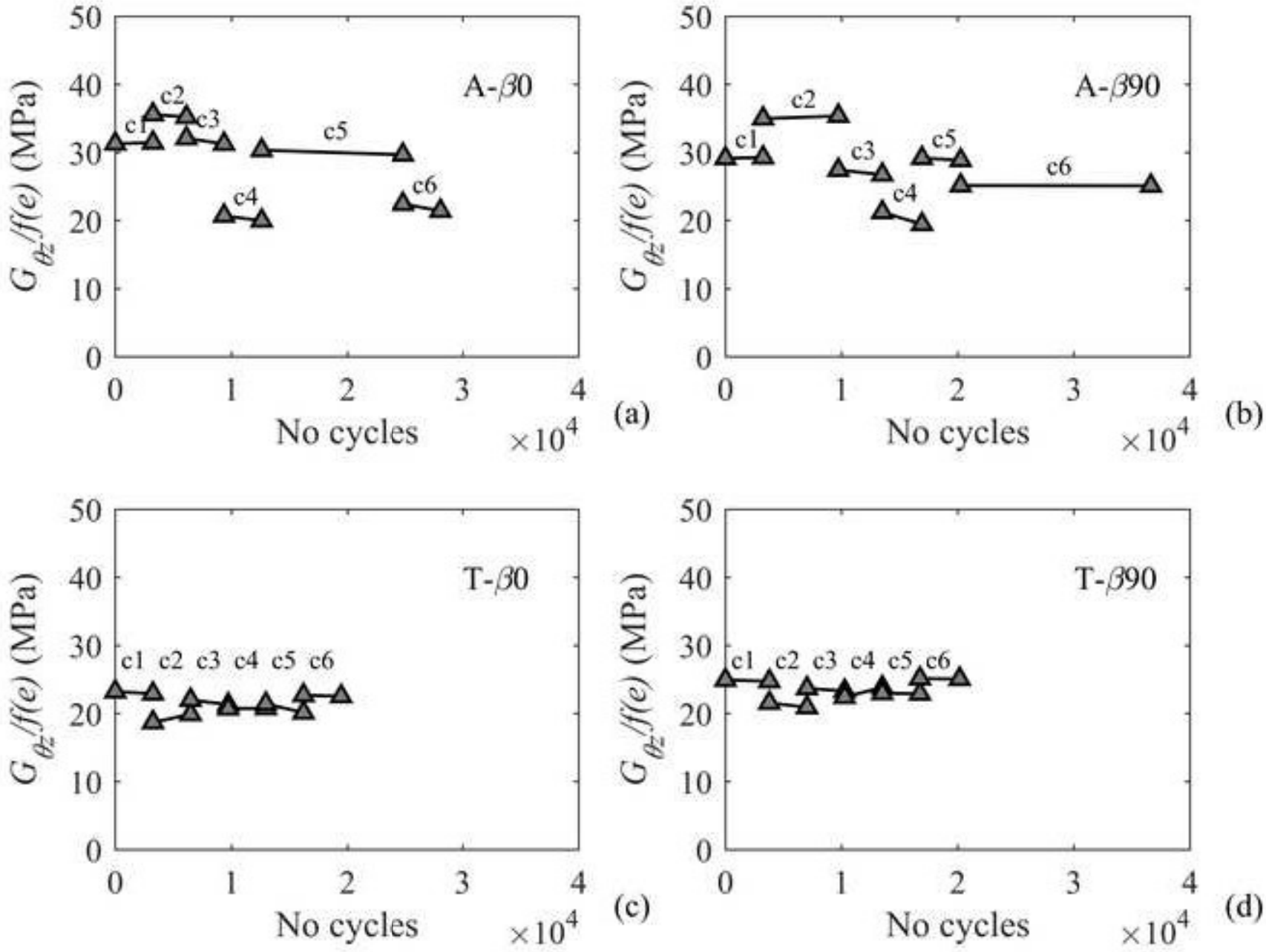

Figure 12

Click here to access/download;Figure;Figure 12.tif

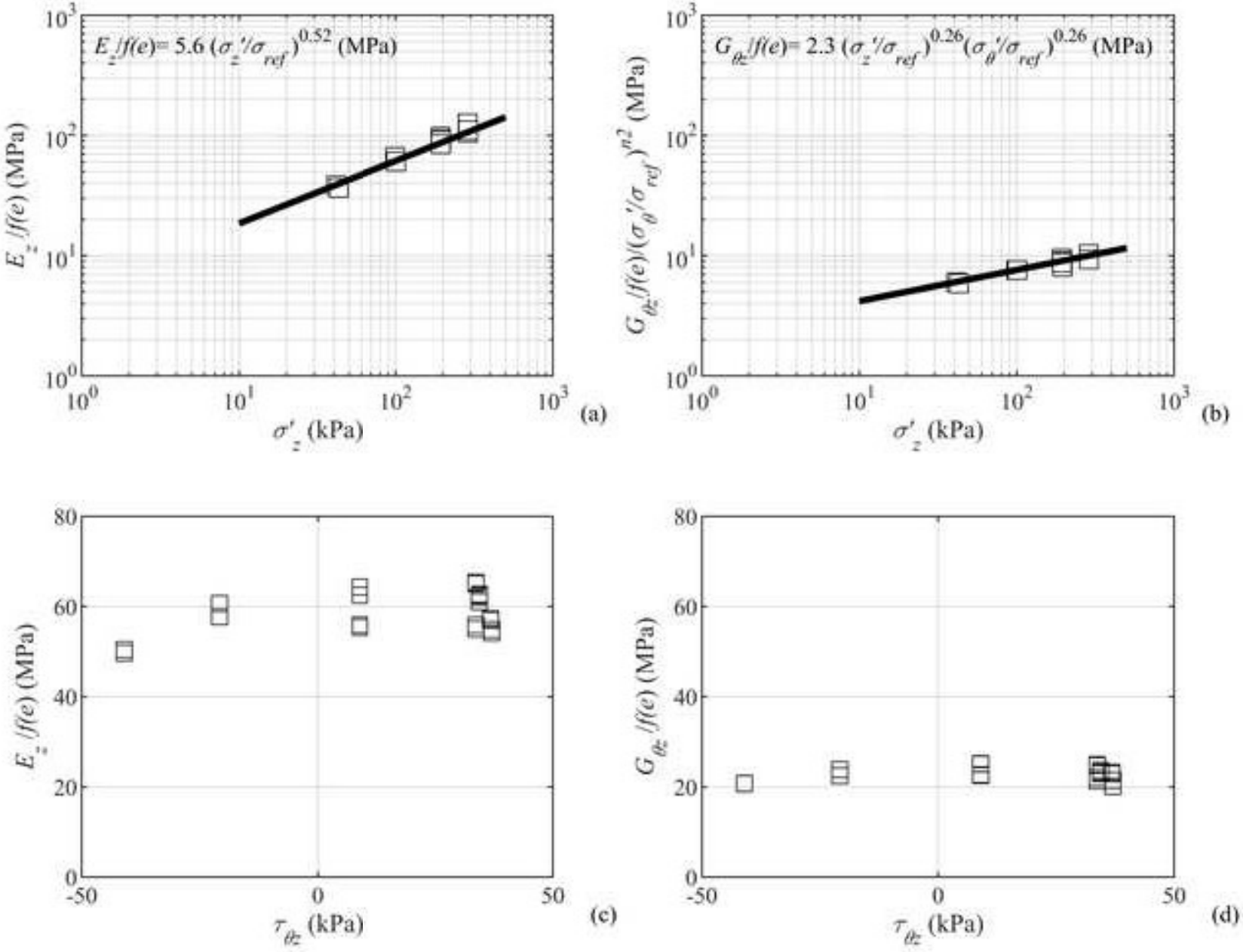

Figure 13

Click here to access/download;Figure;Figure 13.pptx

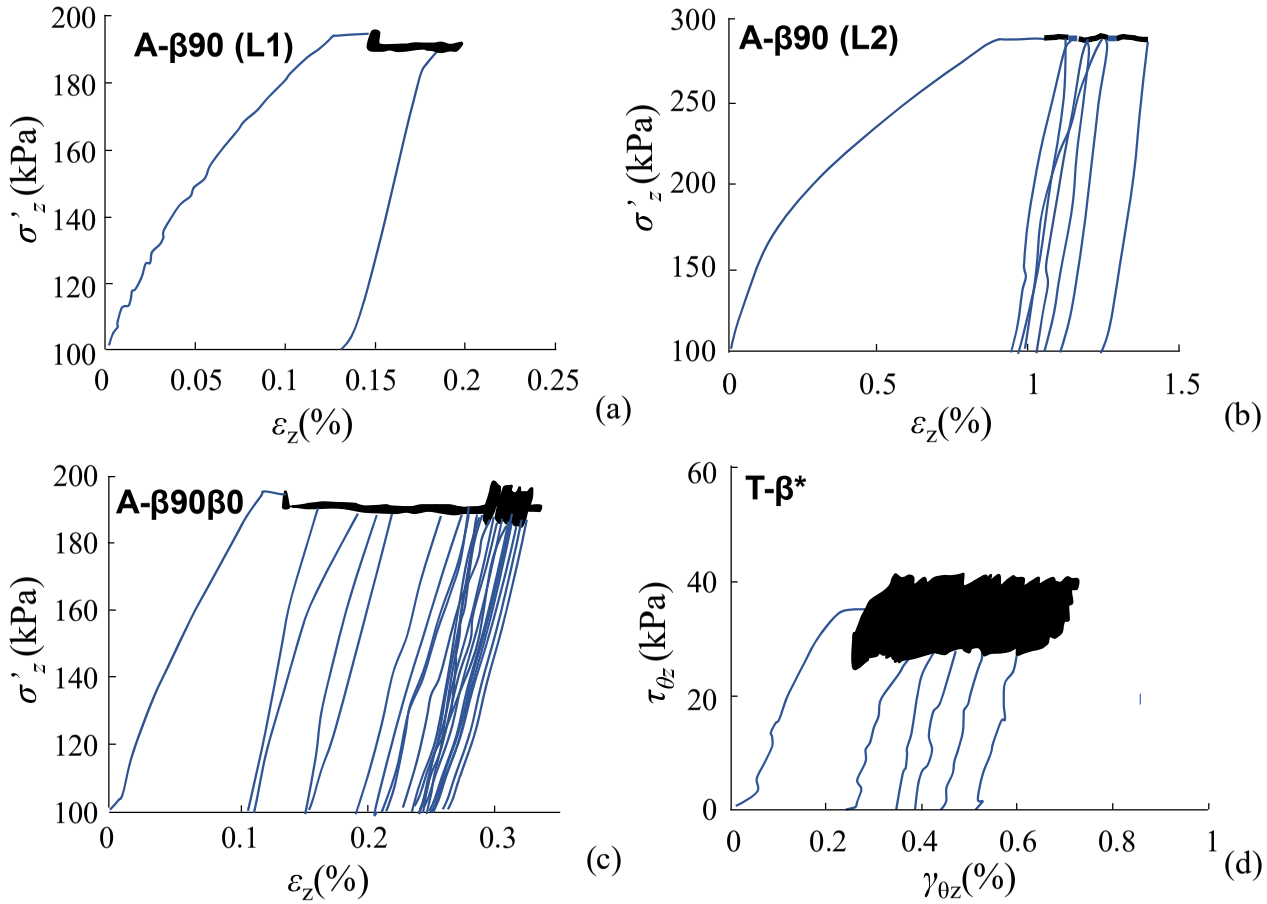

Public

Figure 14

Click here to access/download;Figure;Figure 14.tif

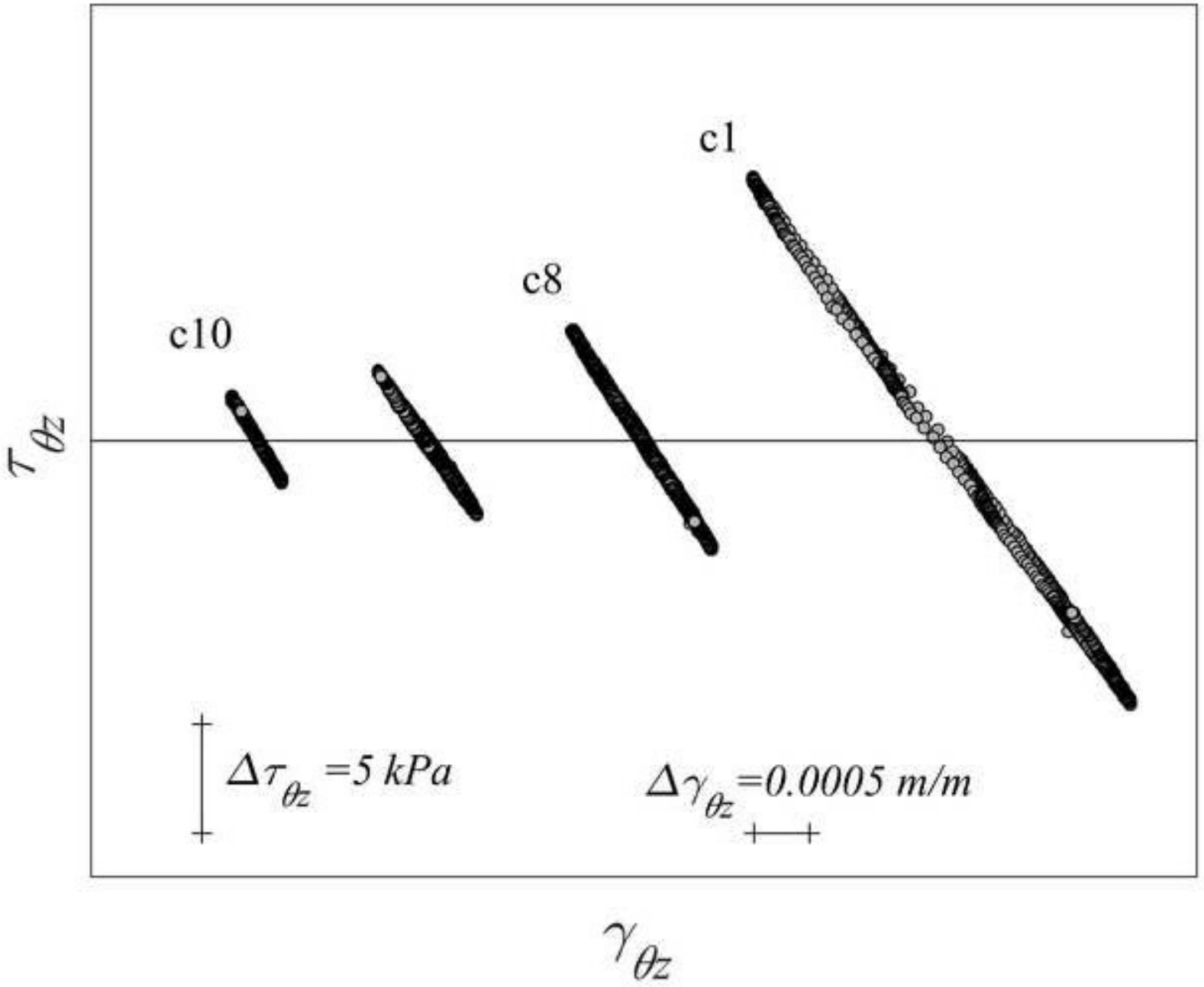

Figure 15

Click here to access/download;Figure;Figure 15.tif

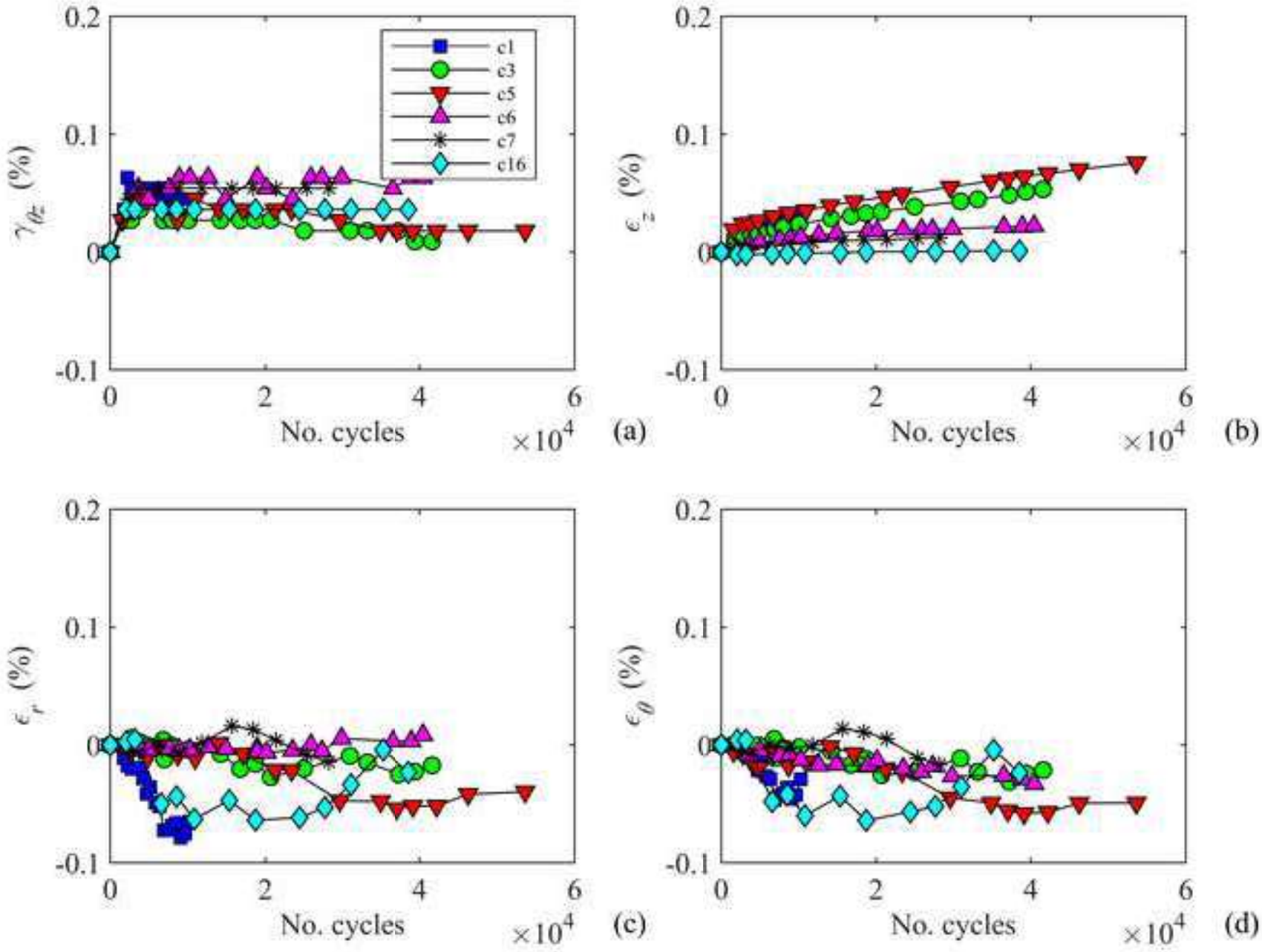

Figure 16a

Click here to access/download;Figure;Figure 16a.tif

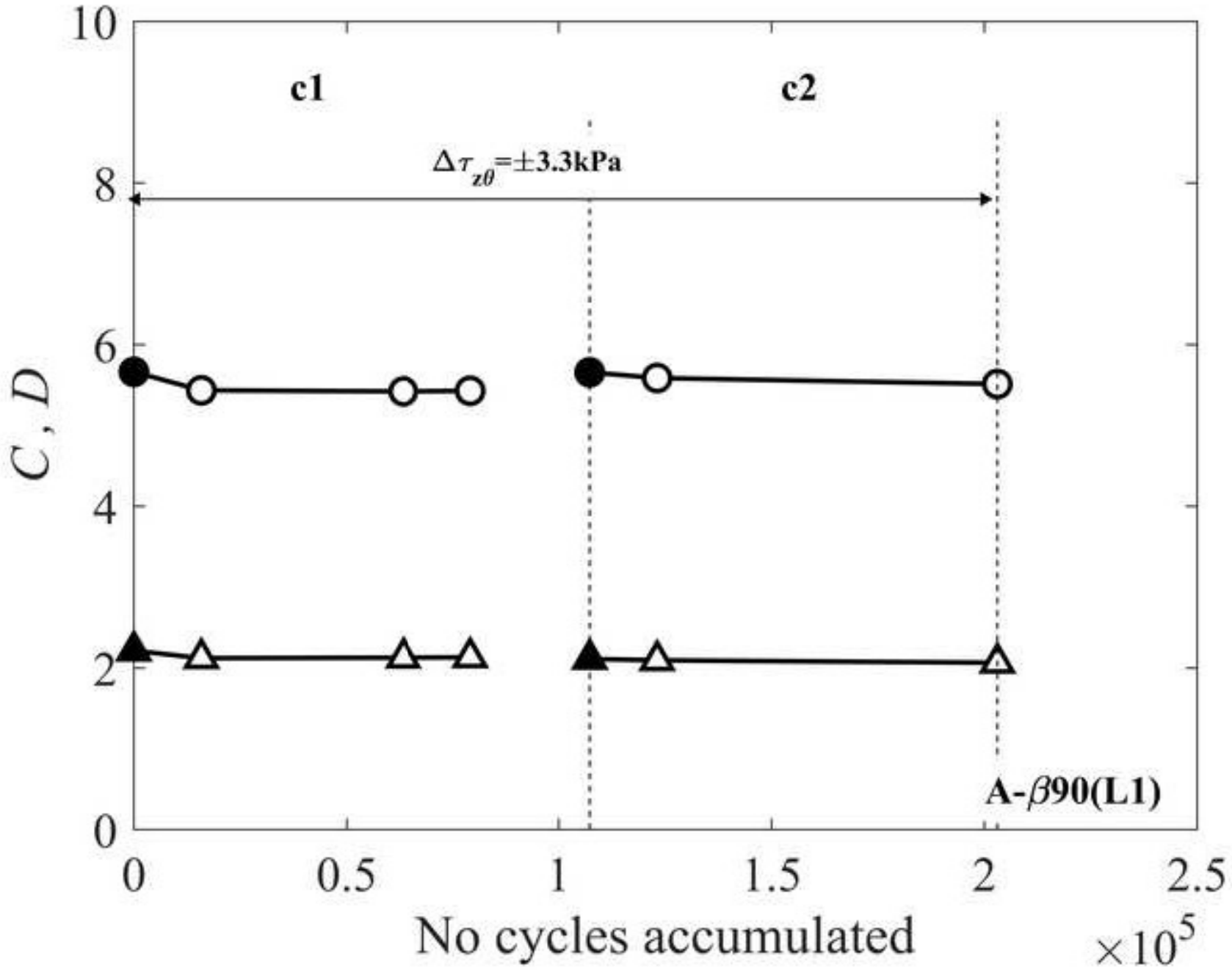

Figure 16b

Click here to access/download;Figure;Figure 16b.tif

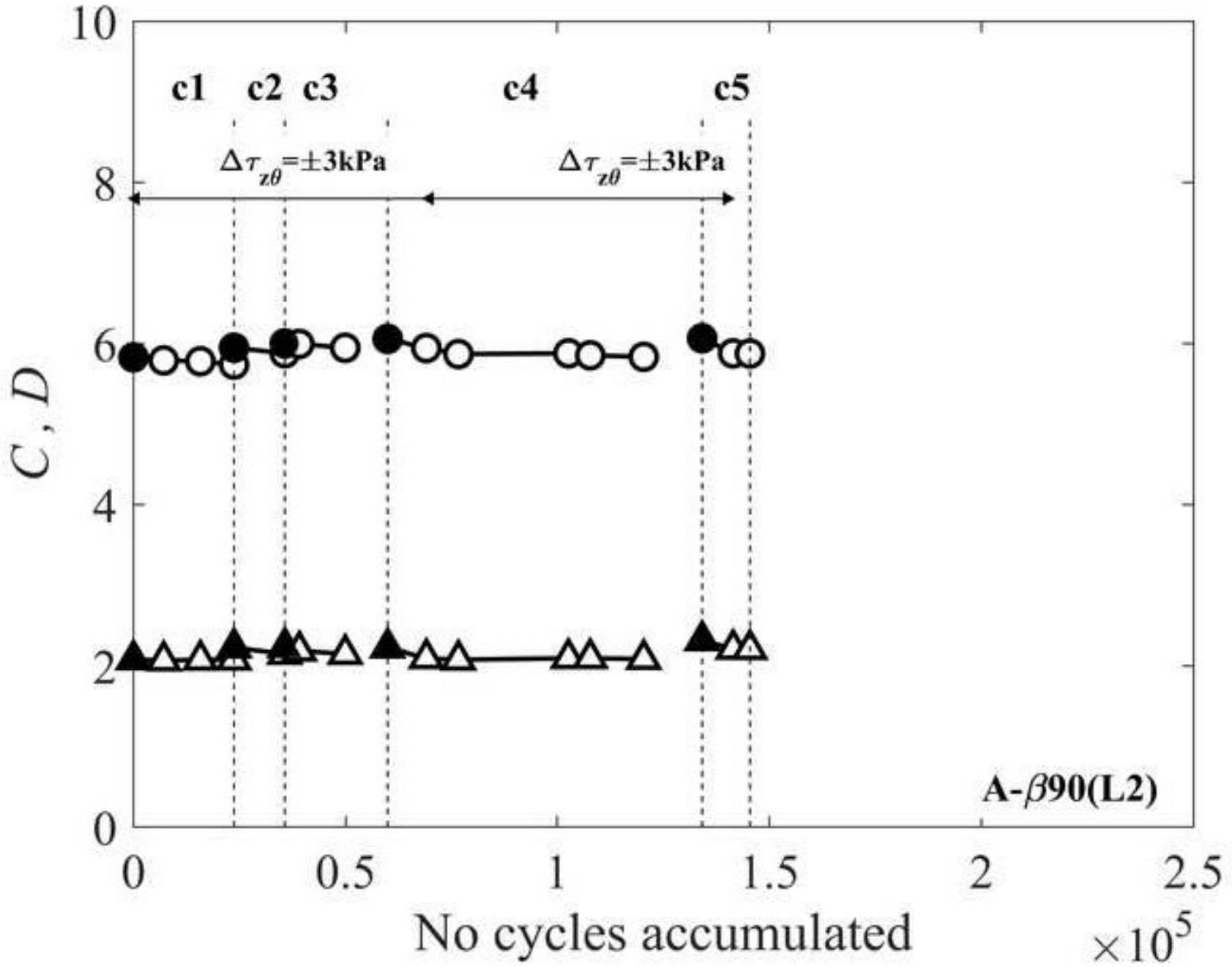

Figure 16c

Click here to access/download;Figure;Figure 16c.tif

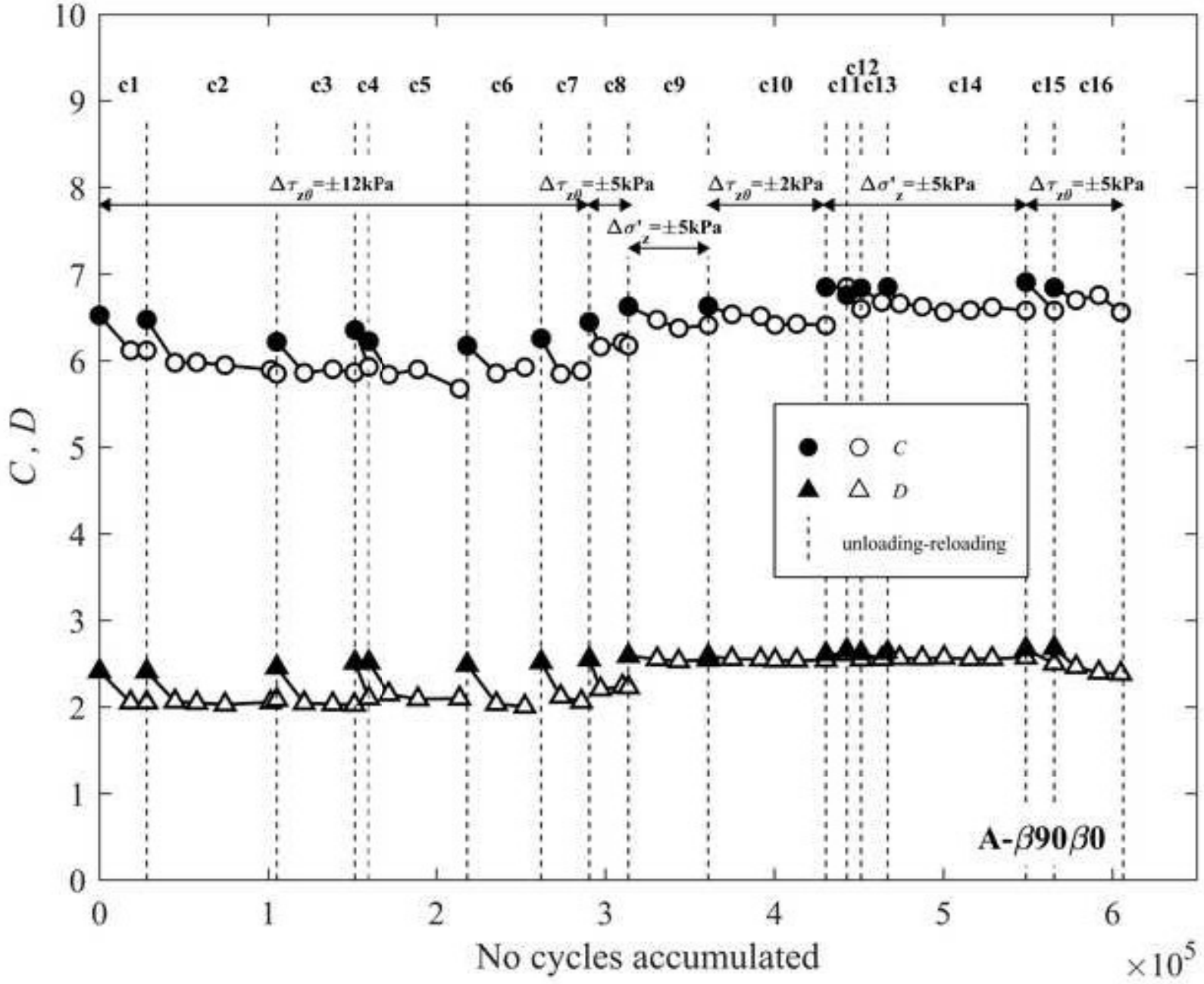

Figure 16d

Click here to access/download;Figure;Figure 16d.tif

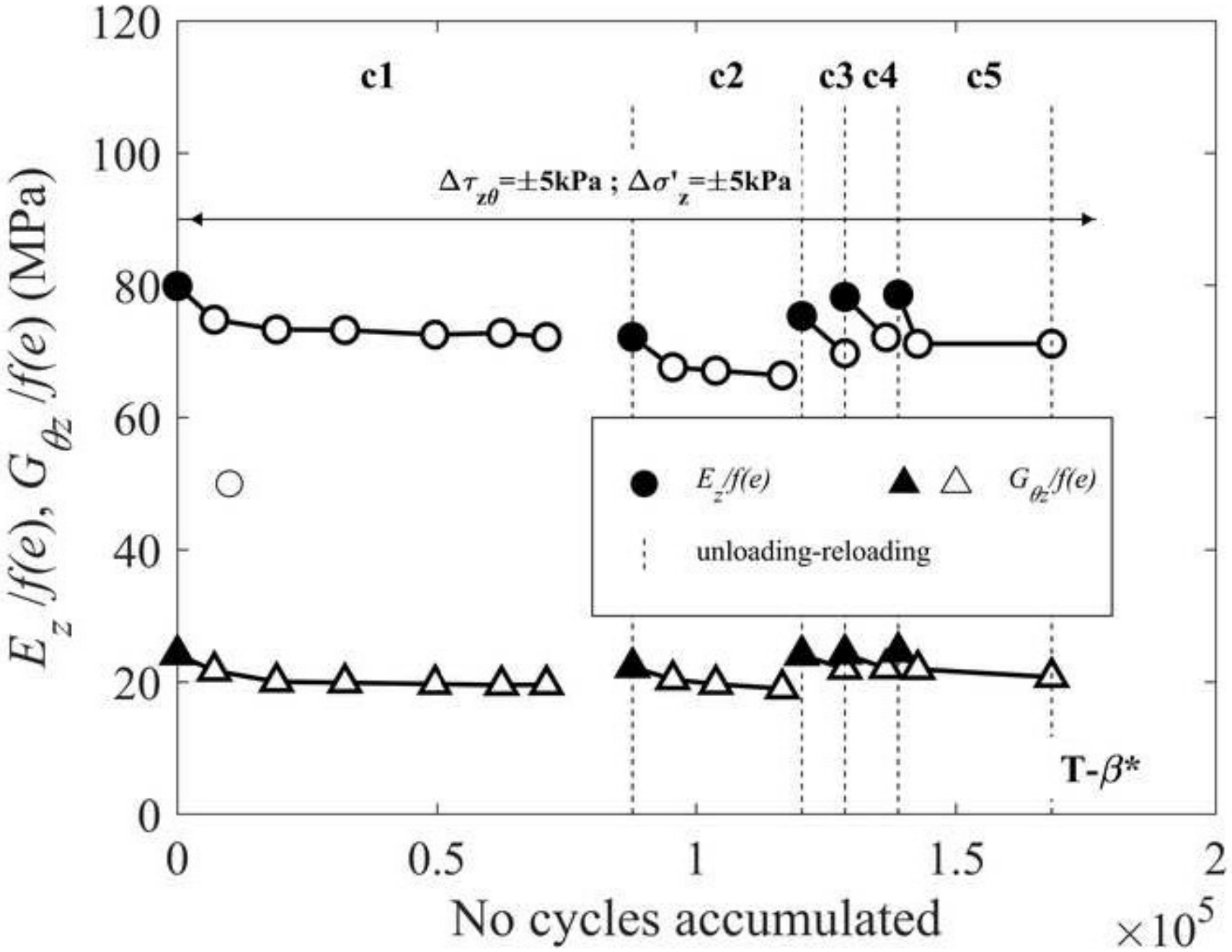

Figure 17

Click here to access/download;Figure;Figure 17.tif

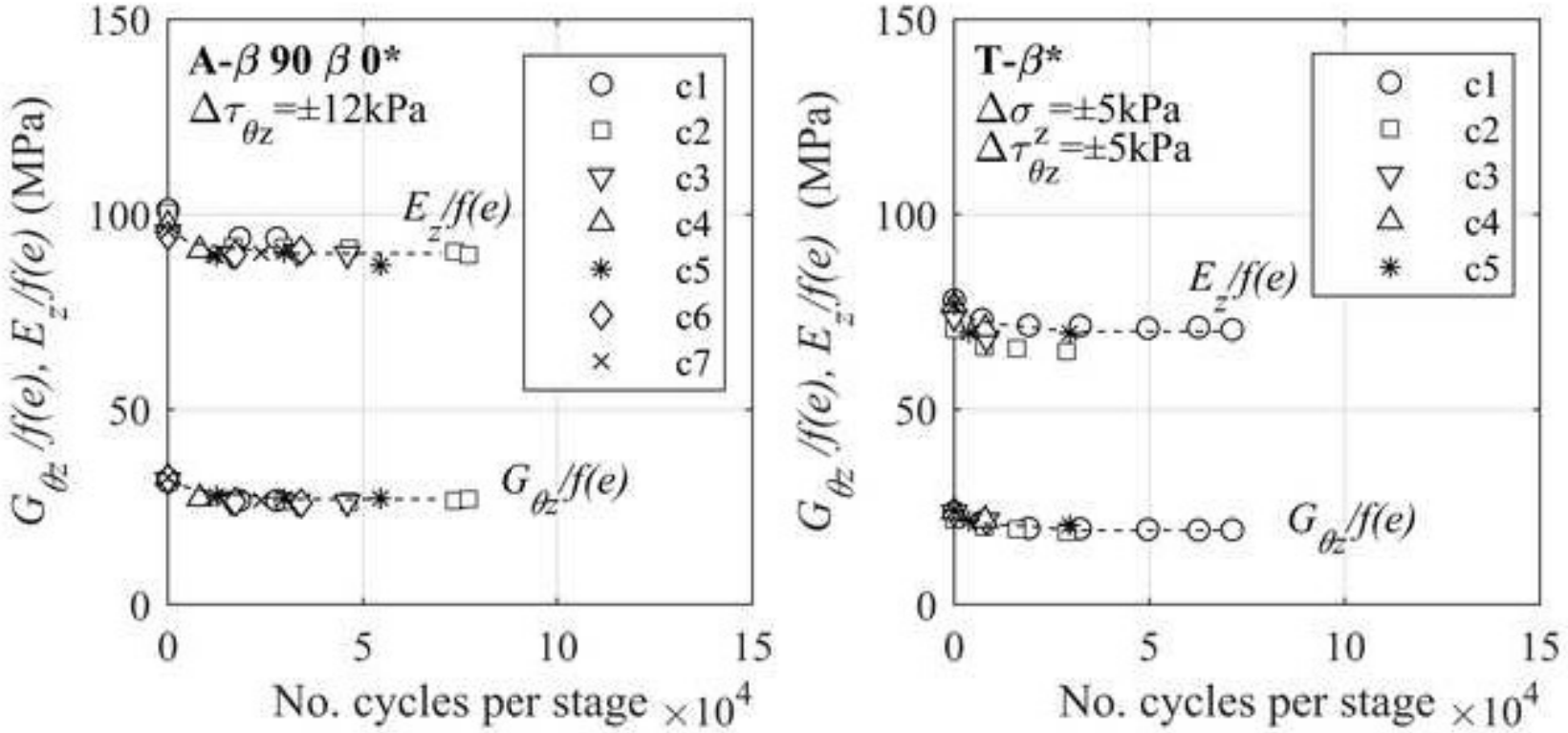

Figure 18a

Click here to access/download;Figure;Figure 18a.tif

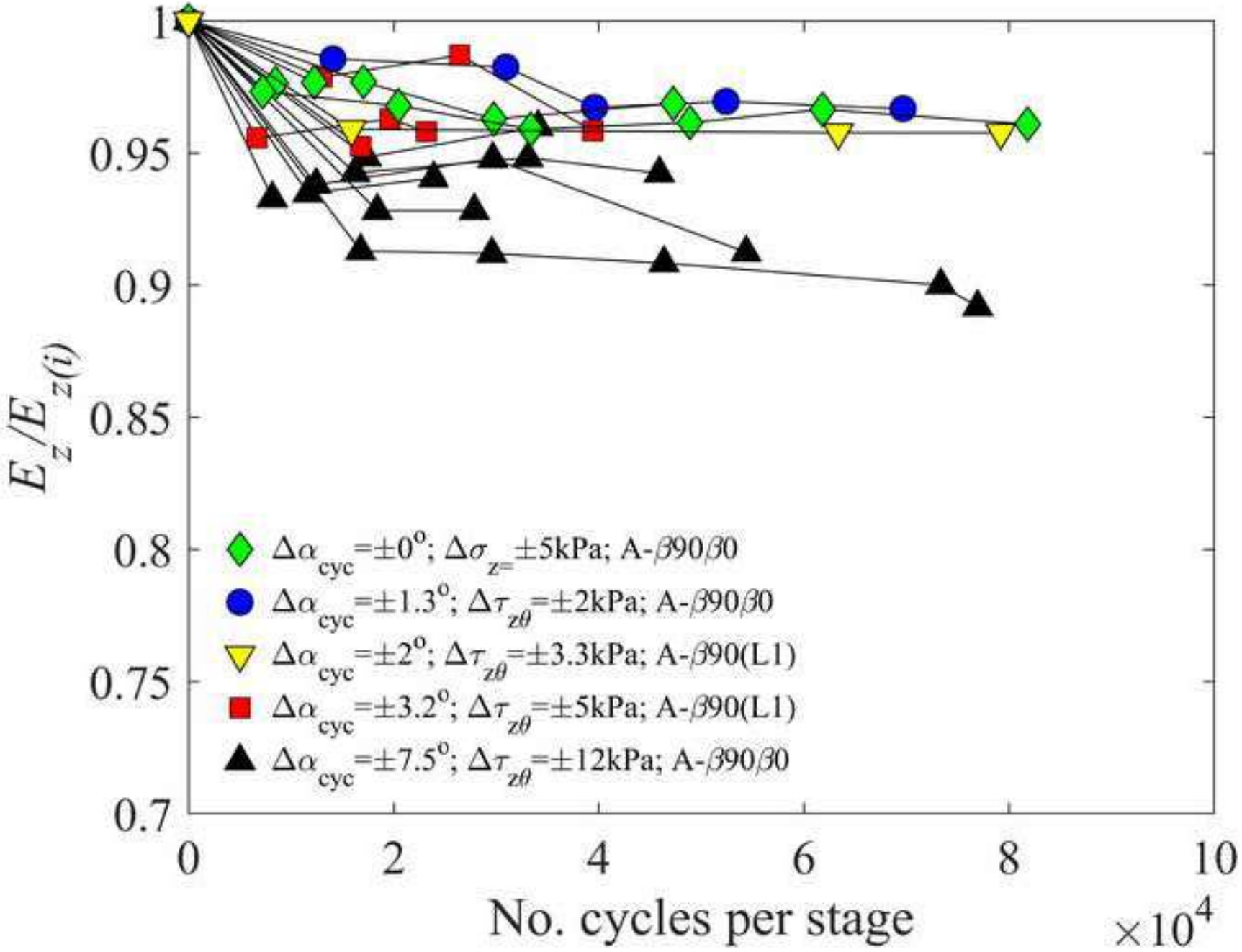

Figure 18b

Click here to access/download;Figure;Figure 18b.tif

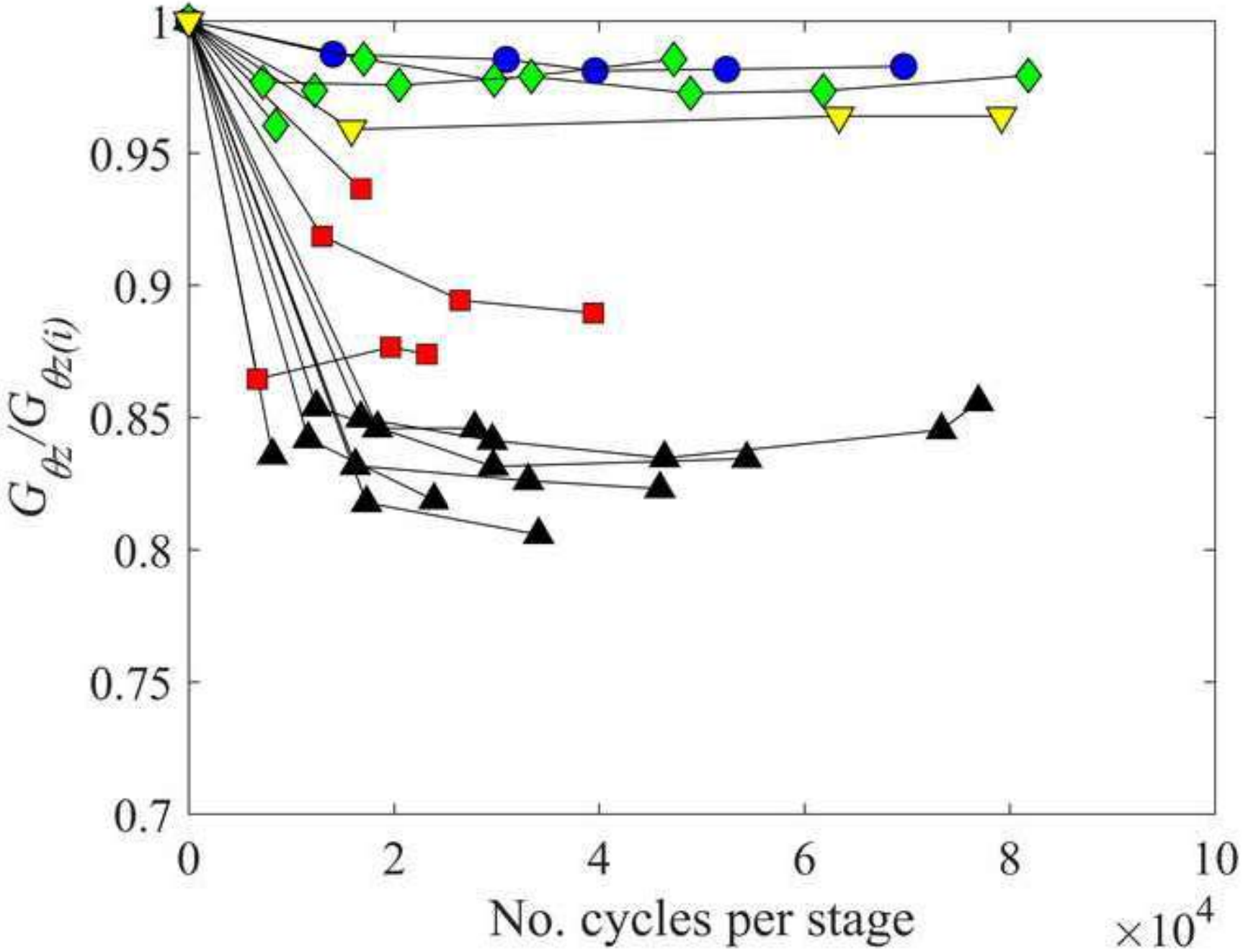

Figure 19a

Click here to access/download;Figure;Figure 19a.tif

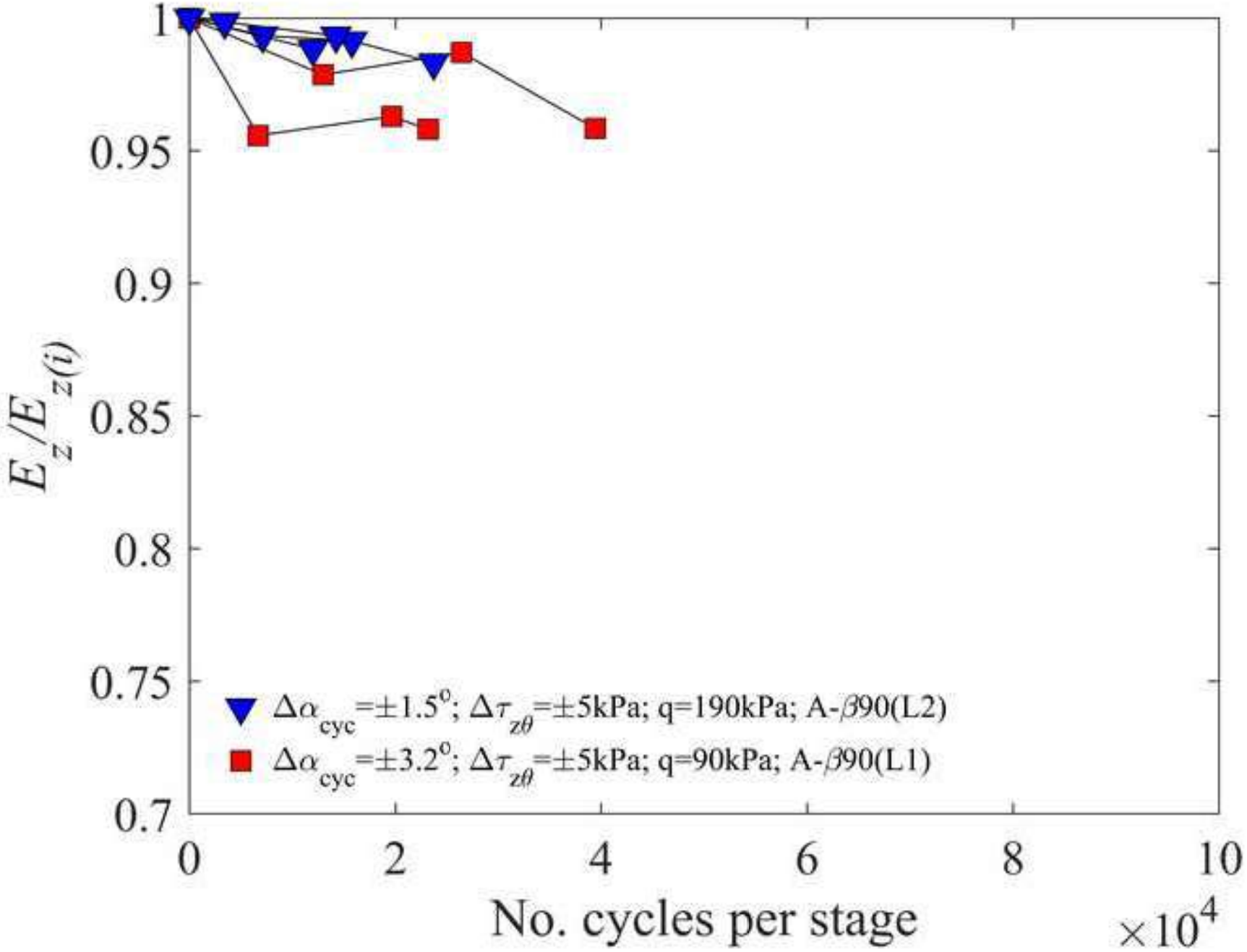

Figure 19b

Click here to access/download;Figure;Figure 19b.tif

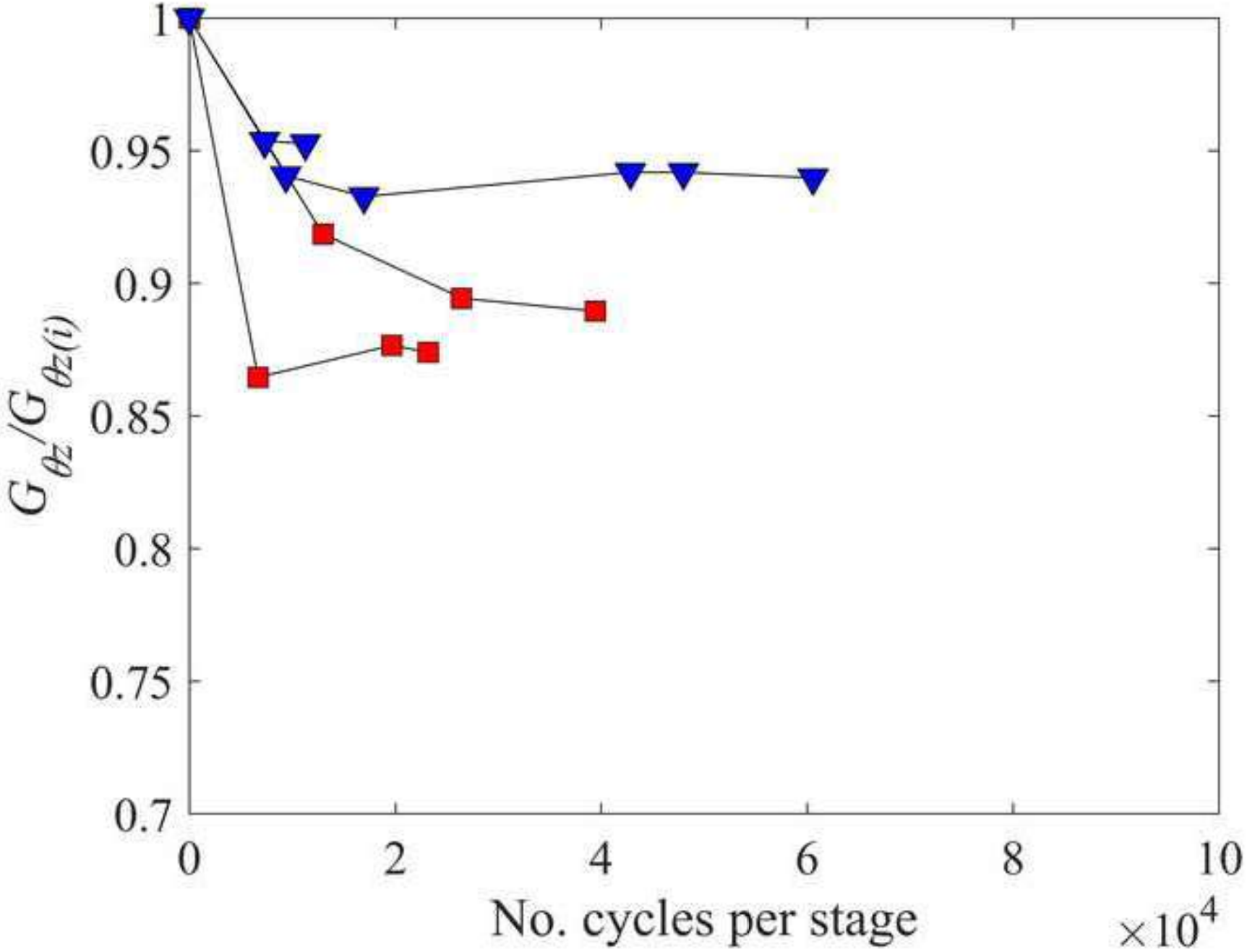

Figure 20a

Click here to access/download;Figure;Figure 20a.tif

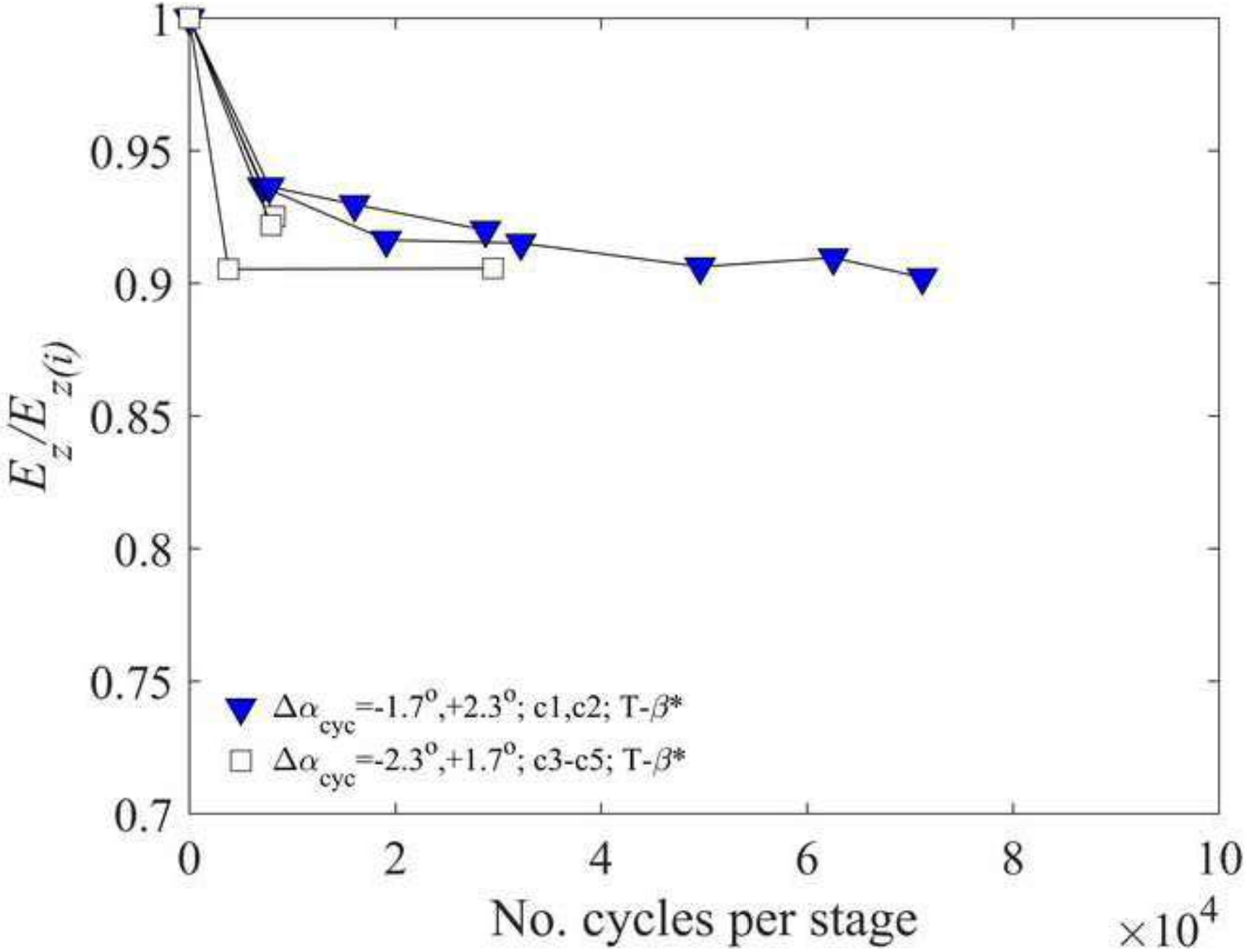

Figure 20b

Click here to access/download;Figure;Figure 20b.tif

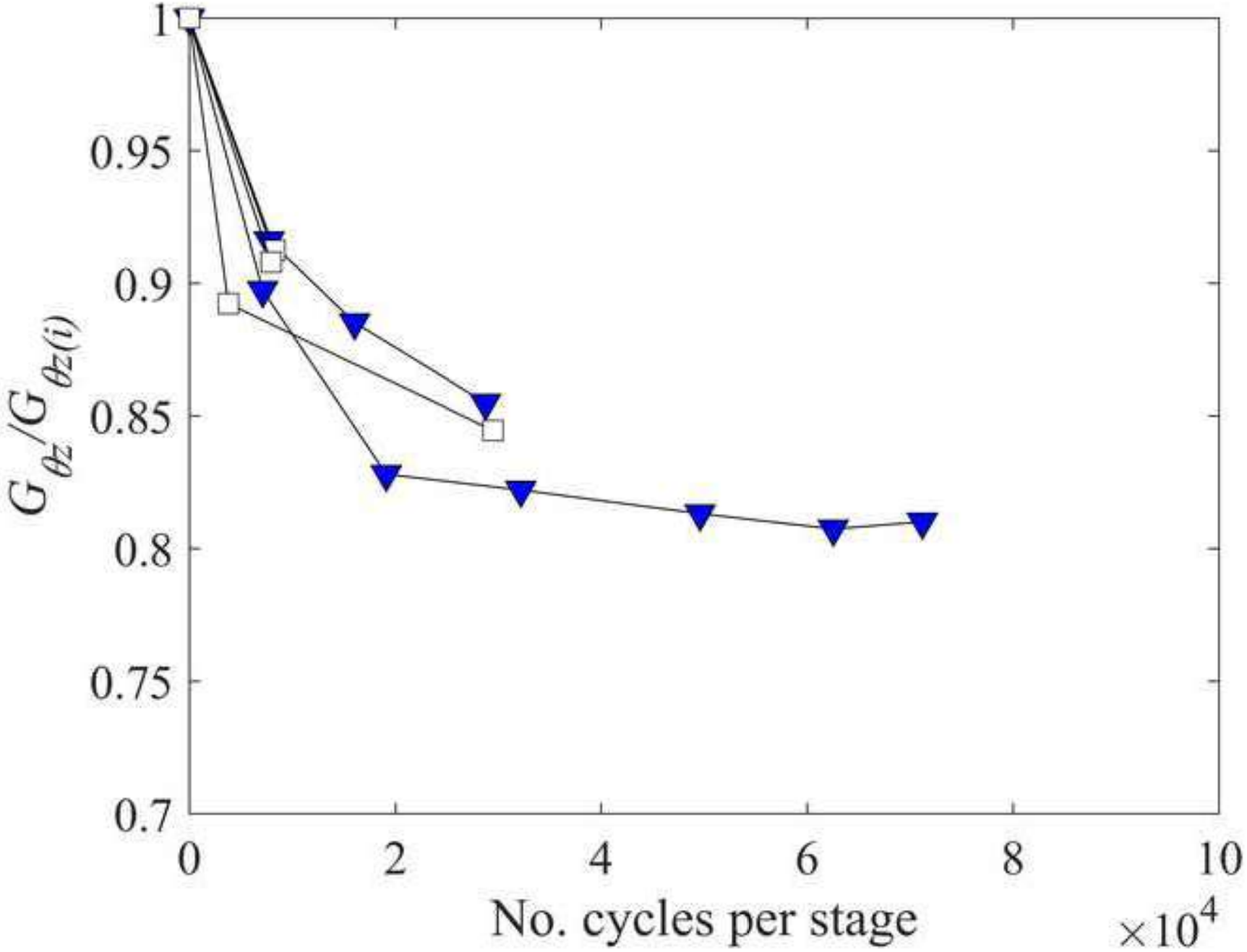

Figure 21

Click here to access/download;Figure;Figure 21.tif

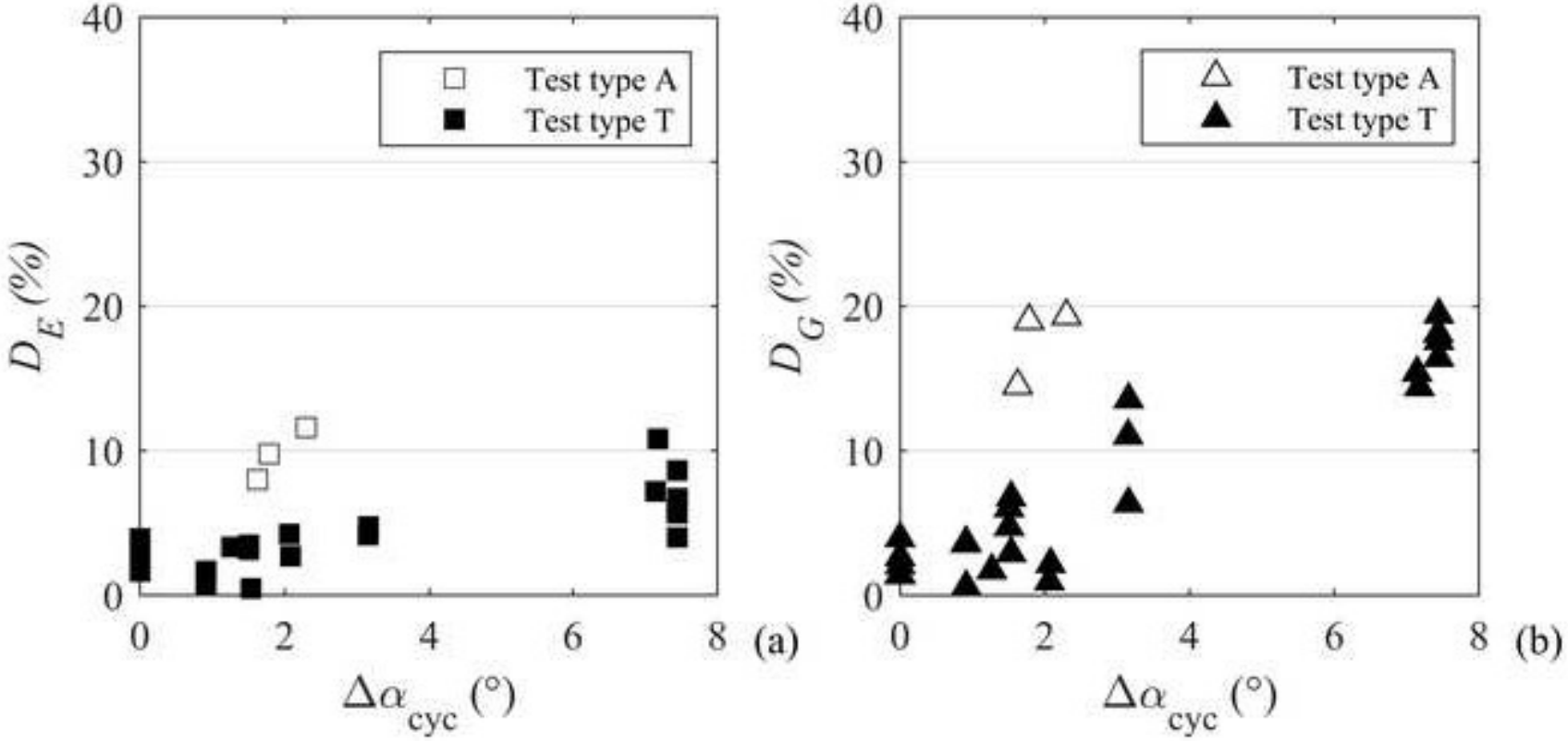

Figure 22

Click here to access/download;Figure;Figure 22.tif